

0361

Public reporting burden for this collection of information is estimated to average 1 hour per response, including gathering and maintaining the data needed, and completing and reviewing the collection of information. Send collection of information, including suggestions for reducing this burden, to Washington Headquarters Services, Directorate for Information Operations and Reports, 1215 Jefferson Davis Highway, Suite 1204, Arlington, VA 22202-4302, and to the Office of Management and Budget, Paperwork Project, Washington, DC 20503.

95,
his
on

1. AGENCY USE ONLY (Leave blank)		2. REPORT DATE	3. REPORT TYPE AND DATES COVERED 15 Feb 98 to 30 Nov 00 Final	
4. TITLE AND SUBTITLE Micromirror Arrays for High Energy Applications			5. FUNDING NUMBERS 61102F 2301/AV	
6. AUTHOR(S) Professor Bright				
7. PERFORMING ORGANIZATION NAME(S) AND ADDRESS(ES) University of Colorado 206 Armory Campus Box B-19 Boulder, CO 80309-0019			8. PERFORMING ORGANIZATION REPORT NUMBER	
9. SPONSORING/MONITORING AGENCY NAME(S) AND ADDRESS(ES) AFOSR/NE 801 North Randolph Street Rm 732 Arlington, VA 22203-1977			10. SPONSORING/MONITORING AGENCY REPORT NUMBER F49620-98-1-0291	
11. SUPPLEMENTARY NOTES				
12a. DISTRIBUTION AVAILABILITY STATEMENT APPROVAL FOR PUBLIC RELEASE; DISTRIBUTION UNLIMITED			12b. DISTRIBUTION CODE	
<p style="text-align: center;">AIR FORCE OFFICE OF SCIENTIFIC RESEARCH (AFOSR) NOTICE OF TRANSMITTAL DTIC. THIS TECHNICAL REPORT HAS BEEN REVIEWED AND IS APPROVED FOR PUBLIC RELEASE LAW AFR 190-12. DISTRIBUTION IS UNLIMITED.</p>				
13. ABSTRACT (Maximum 200 words) The ability to control the phase of a propagating optical wave front is a key enabling technology for a host of scientific, commercial, medical, and defense applications. The objectives of this project are to advance the state of the art of optical MEMS by addressing the following critical development issues: dynamic range, frequency response, aperture size, and optical power handling ability of micromirrors for thermal lensing compensation in lasing systems and optical beam steering. The research includes design, detailed modeling, simulation and experimental investigation of electro-mechanical behavior and optical power handling ability of micromirrors devices.				
14. SUBJECT TERMS 20010625 124			15. NUMBER OF PAGES	
			16. PRICE CODE	
17. SECURITY CLASSIFICATION OF REPORT UNCLASSIFIED	18. SECURITY CLASSIFICATION OF THIS PAGE UNCLASSIFIED	19. SECURITY CLASSIFICATION OF ABSTRACT UNCLASSIFIED	20. LIMITATION OF ABSTRACT UL	

NE

MICROMIRROR ARRAYS FOR HIGH ENERGY APPLICATIONS

GRANT NO: F49620-98-1-0291

FINAL REPORT

FOR THE PERIOD 2/15/98 - 11/30/00

SUBMITTED TO

DR. HOWARD R. SCHLOSSBERG, AFOSR/NE

TEL: (703) 696-7549; FAX: (703) 696-8481

E-mail: howard.schlossberg@afosr.af.mil

801 North Randolph Street, Room 732

Arlington VA 22203-1977

University of Colorado at Boulder

Technical Contacts

Dr. Victor M. Bright, Principal Investigator

Dr. Y. C. Lee, Co-principal Investigator

NSF Center for Advanced Manufacturing and Packaging of

Microwave, Optical and Digital Electronics

University of Colorado, Boulder, CO 80309-0427

(303) 735-1734 (phone), (303) 492-3498 (FAX)

victor.bright@colorado.edu (e-mail)

<http://mems.colorado.edu>

Administrative Contact

Mr. Laurence Nelson, Director

Office of Contracts and Grants

University of Colorado, Boulder, CO 80309-0013

(303) 492-2695 (phone); (303) 492-6421 (FAX)

larry.nelson@colorado.edu (e-mail)

Grant Period: 2/15/98 to 11/30/00

SUMMARY OF RESEARCH OBJECTIVES

The ability to control the phase of a propagating optical wave front is a key enabling technology for a host of scientific, commercial, medical, and defense applications. By controlling the phase of a propagating beam it is possible to correct aberrations in optical systems, control the shape of a focused laser beam, and redirect the laser beam. Scientific and defense applications include high speed optical wave front control for correcting atmospheric turbulence effects for astronomy and space surveillance to provide higher resolution imagery, and control of fixed aberrations in optical systems to allow the development of simpler lens and mirror arrangements. Commercial applications for optical wave front control include beam steering for High Definition Television; solid state device focus control for camcorders; beam quality control for line-of-sight laser communications; and optical interconnects between high speed electronic modules. Medical applications for optical wave front control technology include laser eye surgery. Micro-electro-mechanical systems (MEMS) offer a novel and cost effective device technology for controlling the phase of a propagating optical wave front. MEMS are micro mechanical devices whose position can be electrically controlled. The use of MEMS for atmospheric aberration correction is an example of low optical power application. Other potential applications include compensation for thermal lensing in lasing materials and optical beam steering. These higher power applications represent a challenging frontier for MEMS research and development.

The objectives of this project are to advance the state of the art of optical MEMS by addressing the following critical development issues: dynamic range, frequency response, aperture size, and optical power handling ability of micromirrors for thermal lensing compensation in lasing systems and optical beam steering. The research includes design, detailed modeling, simulation and experimental investigation of electro-mechanical behavior and optical power handling ability of micromirror devices.

SUMMARY OF ACCOMPLISHMENTS

1. FLIP-CHIP LENSLET INTEGRATED MICRO-ELECTRO-MECHANICAL DEFORMABLE MICROMIRROR ARRAY (LMEM-DM)

Flip chip assembly technology offers a reliable and advanced packaging approach for hybrid assembly of micromachined optical components. We used flip chip technology to integrate microlens arrays with surface micromachined segmented deformable micromirrors. 12x12 electrostatic micromirror arrays were fabricated through a commercial surface micromachining process and integrated with polymer and glass microlenses. The Photo-BCB resins, which are photo-sensitive polymers, have been used to fabricate the polymer microlenses. 12x12 element polymer microlens arrays of various focal length have been fabricated on glass substrates. Moreover, a commercial glass microlens array was also integrated on a deformable micromirror. A refractive lenslet array is positioned directly over the micromirror. A spacer is used to precisely define the gap between the micromirror and lenslet chips. A UV-curable epoxy is used to secure the spacer. The use of a lenslet to focus the incoming laser beam onto the reflective surface of a micromirror substantially increases optical fill factor of the micromirror array. For mirror deflections much smaller than the lenslet focal length, the lenslet/micromirror combination behaves as a phase-only modulating optical element. The hybrid lenslet/MEMS arrays thus serve as rugged, compact optical elements for the beam steering, beam shaping, and aberration correction applications.

1.1 12x12 Electrostatic Piston Micromirror Array

The MEMS deformable mirror is comprised of 128 individually electrostatically controlled micromirror elements on a 12x12 square grid array (16 elements; 4 elements (2x2) in each corner are inactive). The devices were fabricated through the commercially available Multi-User MEMS Process (MUMPs) [<http://www.memsrus.com/cronos/svcs/mumps.html>]. This is a three-layer surface-micromachining polycrystalline silicon (polysilicon) process. The lowest polysilicon layer, POLY0, is non-releasable and is used for address electrodes and local wiring. The upper two polysilicon layers, POLY1 and POLY2, can be released to form the mechanical structure. Two sacrificial oxide layers are deposited between the two polysilicon layers and are etched away to release the mechanical layers that are used to form the flexures and suspended mirror. The gold is deposited on the top of POLY2 layer to form the reflective surface, low resistance wiring and bond pads. The reflective gold mirror is a circle shape of 74 μm in diameter. The 250 μm center-to-center spacing of the mirrors in array is designed to match a commercial refractive lenslet array obtained from Nippon Sheet Glass Company. There are 4 flexures and 4 dimples to protect the mirror during the snap through effect. The POLY1 flexures are 12 μm wide and 155 μm long. The stacked polysilicon structure is used in the upper electrode with trapped oxide polysilicon structure used in the active area underneath mirror surface. The benefit to use trapped oxide polysilicon layer underneath the mirror surface is to reduce the surface curvature due to the residual tensile stress in the gold metallization and compressive stress in the POLY2 layer. Interferometric microscope measurement of undeflected micromirror surface shows the curvature less than 62 nm which is adequate for adaptive optics application ($\approx \lambda/10$ optical flatness assuming HeNe light) as shown in Figure 1. Figure 2 shows the scanning electron micrographs (SEMs) of an array and a single micromirror element. Each element is individually addressable via POLY0 wires that run under the support structure so that topology induced in the overlying POLY2 layer does not effected the flatness of the active mirror surfaces or the stiffness of the flexures.

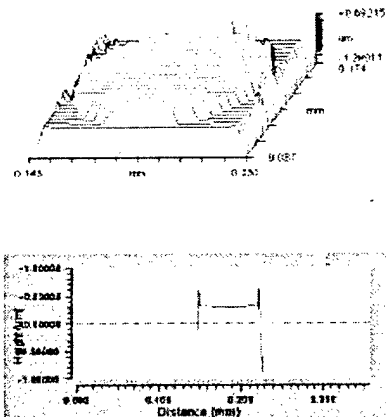


Figure 1. Surface profile of the micromirror.

The deflection, d , of each mirror is controlled by an electrostatic mechanism. The electric voltage V is applied between the moving mirror plate and the underlying address electrode. The nonlinear relation between mirror deflection and the applied voltage is characterized by $d = kV^2$. The value of k measured through the interferometric microscope is 365 nm/V^2 . Electrostatic piston devices exhibit “snapthrough instability” behavior when deflection, d , is one third of the electrostatic gap. At this point the linear restoring force of the flexures cannot balance the rapidly increasing nonlinear electrostatic force, and the micromirror is snapped onto the underlying electrode. The dimples on each flexure are designed to avoid destruction of the mirror by protecting the physical contact between the flexures and underlying electrode. By slowly increasing the applied voltage while observing deflection on the interferometric microscope, the snap

through voltage was measured for several mirror elements with the mean value of 11.4 V. The half-wavelength ($632/2=316$ nm) deflection voltage is approximately 9.7 V. From the observation on interferometric microscope, deflecting the micromirror toward the underlying address electrode by applying an electrostatic potential produced no measurable change in mirror curvature.

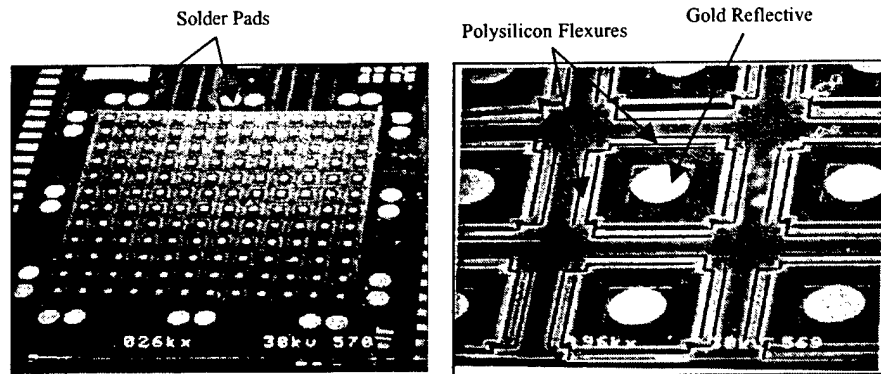


Figure 2. 12x12 electrostatic micromirror array.

1.2. Hybrid Integration of Refractive Lenslet Array

Using the refractive lenslet array to focus the incident light beam onto only the reflective surface of the mirror is one way to greatly improve the effective fill factor with corresponding decrease in static background interference. The 12x12 MEMS deformable mirror was designed specifically for use with an available commercial refractive lenslet array. The two-dimensional planar type micro lens is integrated directly on the top of micromirror array. The Planar Micro Lens (PML) is composed of many micro lens elements formed on a glass substrate by a photolithography and ion-exchange method. A micro lens thus produced is characterized by a hemi spherically distributed index of refraction. Each lens has a circular shape of 0.25 mm in diameter. The 250 μ m center-to-center spacing of the lens array matches with the center-to-center spacing of the micromirror array. The back focal length of the microlens is 0.56 mm. The lenslet array provides approximately 90% light transmission at visible wavelengths.

The hybrid flip chip assembly is applied to integrate the lenslet array on the top of the micromirror array. Two glass spacers of 540 μ m thick and 1mm x 3.5mm are attached to the lenslet array with UV curable epoxy. The released micromirror chip is attached on a fan-out ceramic substrate with conductive epoxy. The ceramic substrate is used to fan out wiring pattern to make the wire bonding pads on the chip compatible with a 144-pin grid array package. The micromirror is electrically connected to the ceramic substrate by wire bonding. Figure 3 shows the concept of lenslet integrated micromirror array.

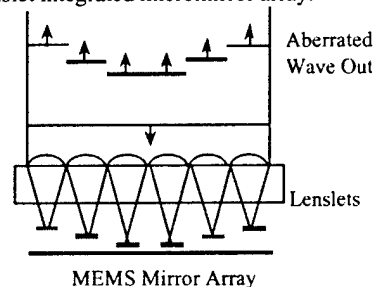


Figure 3. Concept of lenslet integrated micromirror array. The focal point of lenslet array is aligned on the center of the micromirror reflective gold surface.

An epoxy is used to attach the spacer to the micromirror chip. The lenslet array is aligned in X and Y directions using double beam splitters. By this technique, the images of lenslet array and micromirror array can be simultaneously monitored. The alignment is performed manually by adjusting the X and Y position of lenslet chip and rotation of the micromirror chip. The lenslet array is attached and pre-cured under UV light. The Flip Chip assembly is presented in Figure 4. Afterward, the lenslet array integrated micromirror is investigated under interferometric microscope. Fringe patterns observed by interferometric microscope are used to correct possible tilt alignment of lenslet array. The focal point of lenslet is aligned on the center of the micromirror reflective gold surface. The epoxy is then cured firmly. The gap between the microlens and micromirror is controlled by the spacer, and equals to the focal length of the microlens.

The final lenslet array integrated micromirror chip is fixed into a 144 Pin Grid Array (PGA) package using conductive epoxy and electrically connected to package by wire bonding. A photograph of the final packaged device is in Figure 5. The hybrid lenslet/MEMS arrays thus can be fabricated as rugged, compact optical elements for the beam steering, beam shaping, and aberration correction applications.

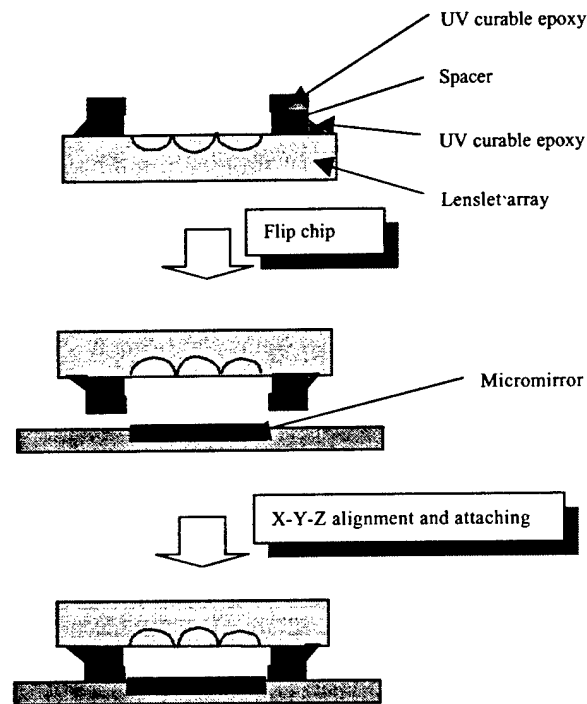


Figure 4. Flip chip assembly process for integration of the lenslet array on top of the micromirror array.

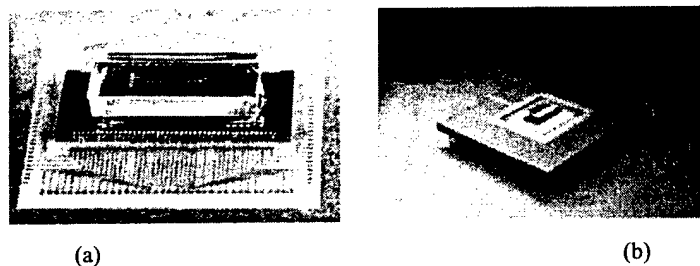


Figure 5. The integrated lenslet array micromirror attached and wire bonded to the fan-out ceramic substrate (a), and the final device packaged in a 144 PGA (b).

1.3 Experimental Results

1.3.1 Mirror deflection

Our deformable mirror is an electrostatically driven device. The mirror deflection is controlled by applied voltage through a nonlinear equation $d = kV^2$, where k is the deflection constant determined by the physical parameters of the device such as the electrode area, dielectric constant of the medium in the gap between electrodes, and the flexure spring constant.

Using the static fringe measurement, the voltage $V_{316} = 9.31$ V for the 316 nm ($\lambda/2$) deflection, which corresponds to full wave modulation, was determined. k is computed by $k = 316 / 9.31^2 = 3.65$ nm/V². The plot of deflection versus applied voltage is shown in Figure 6. The snap-through effect happens when the applied voltage is higher than 11.4 V. The full deflection when snap-through effect exists was measured under interferometric microscope and is equal to 1.387 μ m.

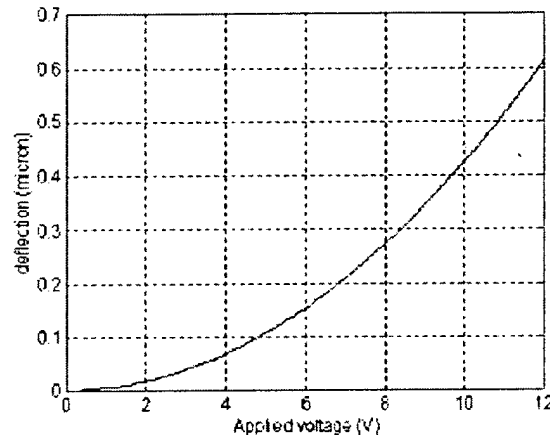


Figure 6. Plot of mirror deflection versus applied voltage for $k = 3.65$ nm/V².

The mirror operating voltage range is established as 9-11.4 V. From known deflection constant k and operating voltage range, we can compute the control voltage for each micromirror element.

1.3.2 Optical setup

The observation of the far-field diffraction pattern obtained from the reflection of a coherent beam off the micromirror array surface is the best way to determine the quality of piston micromirror array. The measured zero order (on-axis) intensity of far-field diffraction or point spread function (PSF) is a function of the mirror surface quality and array fill factor.

The optical experimental setup shown in Figure 7 was used to measure the far-field diffraction pattern of tested LMEM-DM. The collimated 18 mW Helium-Neon (HeNe) laser (wavelength = 632.8 nm) was used as a signal light source. The collimated beam is passed through the spatial filter to obtain a clean light signal and expanded beam. The beam is folded by mirror M_1 into the optical characterization branch. The beam enters a beam splitter (BS1) and is redirected toward the LMEM-DM by passing through a pair of lenses L_1 and L_2 between BS1 and LMEM-DM. This pair of lenses serves to reduce the diameter of beam to fill the controllable mirror surface of LMEM-DM. The packaged LMEM-DM is mounted at the back focal plane of lens L_2 . An iris is located in front of BS1 a focal length away from lens L_1 to control beam diameter. The modified beam from LMEM-DM is reflected back through the afocal telescope (L_1 and L_2), BS1 and

translating lenses L_1 and L_2 . The beam enters a Fourier transforming lens L_F and generates the far-field diffraction. 256×256 pixel CCD camera is used to capture the image of the far field diffraction pattern. Focal lengths of lenses and specification of optical component locations in experimental setup are shown in detail in Table 1 and 2, respectively.

Table 1. Focal Lengths of Lenses Used in the Experimental Setup.

Lens	Focal length (mm)
L_1	250
L_s	500
LL (lenslet)	0.56
L_{t1}, L_{t2}	300
L_F	75.6
L_M	12.7

Table 2. Specifications of Optical Component Locations in the Experimental Setup.

Distance	Nominal Distance (mm)
Iris to L_1	250
L_1 to L_s	750
L_s to LL	500
LL to micromirror	0.56
L_1 to L_{t1}	550
L_{t1} to L_{t2}	600
L_{t2} to L_F	375.6
L_F to L_M	75.6
L_M to CCD camera	90

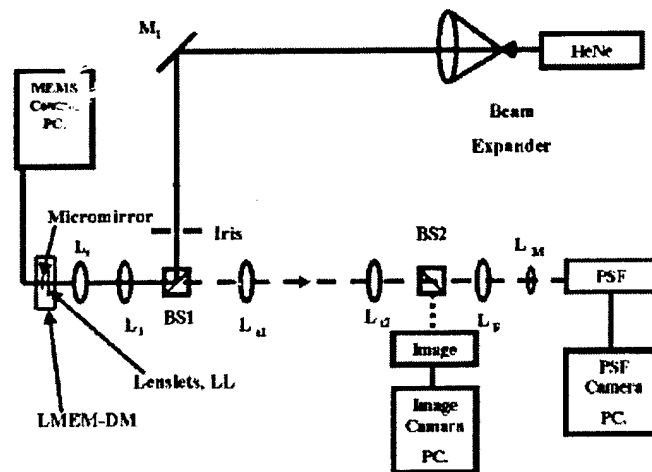


Figure 7. The optical experimental setup used to measure the far-field diffraction pattern of tested lenslet array integrated micromirror.

1.4 Experimental Result and Analysis

1.4.1 PSF of bare micromirror array

Figure 8 shows the far field diffraction pattern for a plane wave reflected from a bare micromirror (no lenslets). The figure shows that the segmented, periodic structure of the micromirror array has diffracted much of the reflected energy into higher orders. Due to the array of square structures of micromirrors, the symmetry array of delta function pattern in x and y direction convoluted with the sinc^2 function pattern is obvious, as predicted.

Since the main lobe energy is significantly lost to higher orders, we expect the peak intensity in the central order to be lower than that for the plane solid mirror reflection. The light illuminates the entire surface of micromirror array including the flexures and other non-reflective surfaces causing the unwanted diffraction pattern to appear around the central PSF as seen in Figure 8.

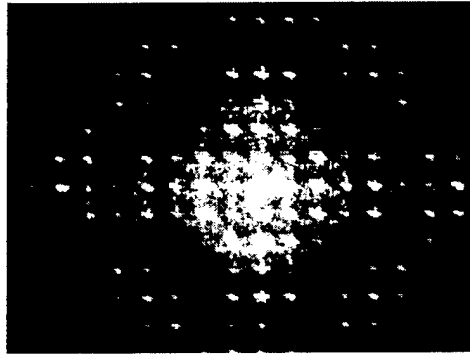


Figure 8. The diffraction pattern of bare micromirror array (no lenslets).

1.4.2 PSF of LMEM-DM

The same test procedure was used for LMEM-DM. A plane wave front is illuminated on the lenslet array. The overall far field diffraction pattern is shown in Figure 9.

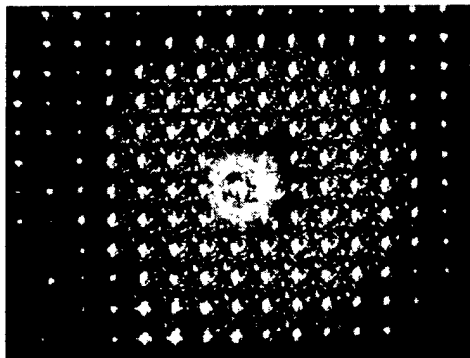
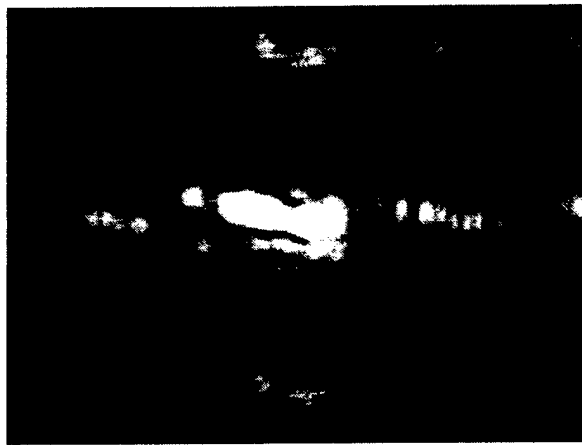
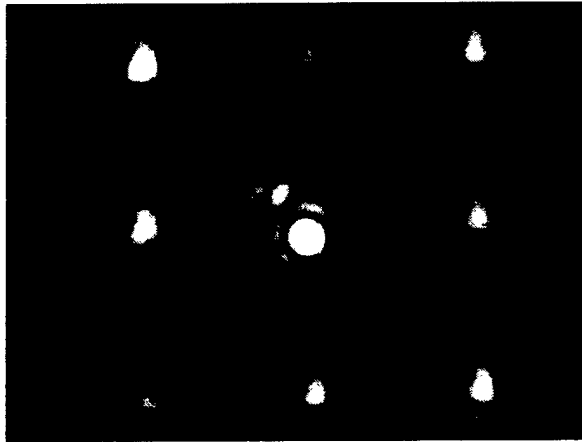


Figure 9. The diffraction pattern of LMEM-DM.

Due to the geometry of lenslet array as two dimensional periodic array of phase modulated circular apertures, the Airy function convoluted with the array of delta function patterns in x and y direction is observed, as expected. Because the light is focused onto micromirror reflective surface only, there is no unwanted diffraction pattern appearing. The far field diffraction pattern is obviously clearer compared to that of bare micromirror array as compared in Figure 10. The static background interference effect due to the non-reflecting parts such as flexures is reduced. In Figure 10, the far field diffraction pattern of bare micromirror consists of the unwanted diffraction pattern located around the central lobe and the blur in higher order lobes. When the lenslet array is integrated onto the micromirror, the far field diffraction pattern is significantly improved. The main central and higher order lobes are focused down as round spots. The static interference pattern around the main lobe disappears. From the measurement, the point spread function (PSF) of main lobe is greatly improved in the intensity of main lobe ($\approx 66\%$ increment) and the Full Width Half Maximum (FWHM) ($\approx 27\%$ reduction).



(a)



(b)

Figure 10. The diffraction pattern in the vicinity of zeroth order of bare micromirror array (a) compared to the LMEM-DM (b).

1.5 SUMMARY OF 12x12 LMEM-DM

The use of a lenslet to focus the incoming laser beam onto the reflective surface of a micromirror substantially increases optical fill factor of the micromirror array. The experimental setup demonstrates the far field diffraction pattern of bare micromirror array compared to that of lenslet integrated micromirror array (LMEM-DM). The experimental results show improvement in the far field diffraction pattern or point spread function (PSF) of the light signal beam. The lenslet array has improved intensity of the main central lobe and Full Width Half Maximum (FWHM) of observed far field diffraction pattern.

Published papers:

- A. Tuantranont, V. M. Bright, W. Zhang and Y. C. Lee, "Flip Chip Integration of Lenslet Arrays on Segmented Deformable Micromirrors," *SPIE* Vol. 3680, pp. 668-678, 1999.
- A. Tuantranont, V. M. Bright, W. Zhang and Y. C. Lee, "Packaging of Lenslet Array on Micromirrors," *SPIE* Vol. 3631, pp. 156-164, 1999.

2. SELF-ALIGNED LENSLET INTEGRATED MEMS-DEFORMABLE MICROMIRROR ARRAY

Lenslet integrated Micro-Electro-Mechanical Deformable Micromirrors (LMEM-DMs) are electrostatic micromirror arrays fabricated through a commercial surface micromachining process and integrated with polymer or glass microlenses. The electronics resins (Photo-BCB) which are photo-sensitive polymers were used to fabricate polymer microlens arrays. 4x4 element photo-BCB Cyclotene microlens arrays were fabricated on a thin quartz substrate. Self-aligned soldering flip-chip assembly is applied to integrate the microlens array directly over the micromirror. The lens/mirror gap is controlled using the reflowed height of solder balls, and the lateral alignment is achieved by the solder self-aligning mechanism. The LMEM-DM is attractive due to its low cost and the low drive voltages. The use of a lenslet to focus the incoming laser beam onto the reflective surface of a micromirror substantially increases overall optical fill factor of the micromirror array. The LMEM-DM provides superior aberration correction with low residual diffraction effects. For mirror motions much smaller than the lenslet focal length, the LMEM-DM behaves as a phase-only modulating optical element. The LMEM-DM thus serves as a rugged, compact optical element for beam steering, beam shaping, and aberration correction applications.

2.1 Fabrication of Polymer Microlens Array

The refractive microlens array was made of the electronics resins (Photo-BCB) which are photo-sensitive polymers. A 4 x 4 element photo-BCB microlens array was fabricated and formed by melting it on a thin quartz substrate. The focal length of the microlens is controlled by deposited polymer thickness. After reflow at certain temperature, the lenses are formed in a spherical shape. The focal length of the microlens is set by controlling the initial thickness of the photo-BCB layer and the diameter of the lens, that are defined by photolithography. The photo-BCB thickness required for a given radius of curvature for the lens may be calculated by equating the volume of spherical portion representing the final lens shape to the volume of a cylinder representing the photo-BCB column before reflow. Photo-BCB works for microlens processing due to its low cure temperature (as low as 200°C), rapid thermal curing (<1 min at 300°C), high solvent resistance and high optical transparency (>90% across the visible spectrum). We thus chose photo-BCB for fabrication of spherical shaped microlens arrays on quartz substrates.

The fabricated photo-BCB microlens arrays have the following parameters:

- Lens element diameter is 80 μm
- Center-to-center spacing is 90 μm
- The centric dome height is 7 μm
- Back focal length is 122 μm

The microlens is fabricated by using photolithography and reflow techniques. The microlens array fabrication steps are shown in Figure 11.

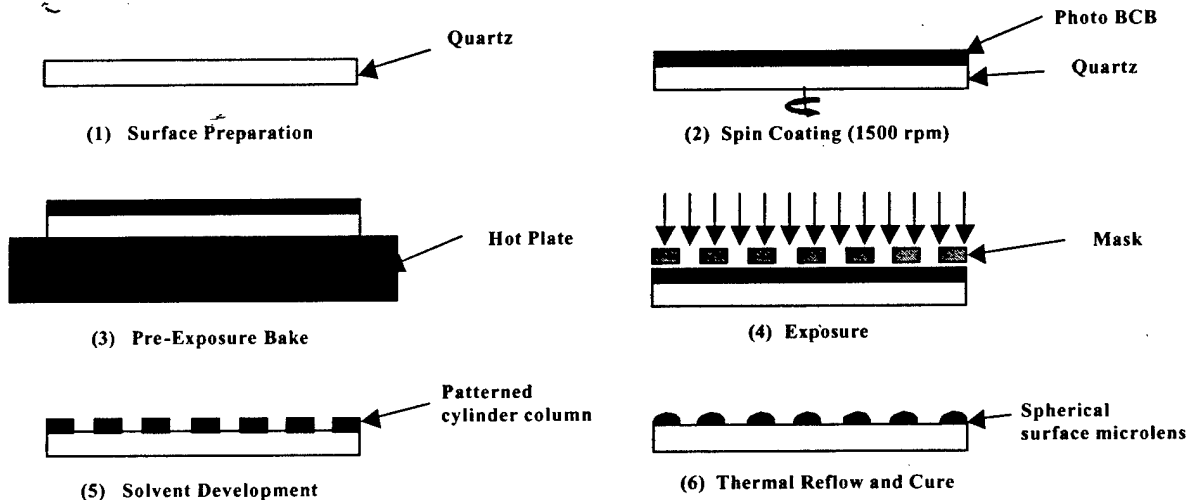


Figure 11. Polymer microlens array fabrication sequence.

2.2 Assembly with Micromirror

The self-aligning solder flip chip assembly is applied to integrate the lenslet array on the top of the micromirror array. This technology offers advantages of low cost, high yield, batch assembly, and self-aligning capability. In particular, the self-alignment mechanism is critical to precision optical assemblies. The use of this technique to integrate lenslet array to MEMS-based micromirror is the novel concept of lenslet array integration. In the self-aligned soldering technique, the surface tension force of molten solder drives the misaligned solder joint to become a well-aligned joint with minimum surface energy. The accurate alignment occurs automatically during the solder reflow. The final alignment accuracy of lenslet array is thus greatly improved. The focal point of a lenslet is aligned on the center of the micromirror reflective gold surface within submicrometer lateral alignment accuracy. A gap between the micromirror and lenslet chip is controlled precisely by the final height of solder joint to be exactly the focal length of the microlens.

The public domain software *Surface Evolver* is modified as a modeling tool for the design of solder joints for self-aligned assemblies [K.F. Harsh, V.M. Bright, Y.C. Lee, "Solder Self-Assembly for Three-Dimensional Micro-electromechanical Systems," *Sensors and Actuators A*, vol. 77, pp. 237-244, 1999]. The software calculates solder shapes with local minimum surface energies and identifies the final shape with global minimum energy.

2.2.1 Modeling of assembly

First, the *Surface Evolver* software was used to calculate the local minimum solder shape. By inputting a user-defined initial surface, the program evolves it toward a minimum energy profile. Numerically, *Surface Evolver* uses a gradient descent on a space of admissible surfaces to try to find a local minimum of energy function. Therefore, solder shape and final gap between microlens chip and micromirror chip are defined by surface energy minimization. The assembly parameters that have to be considered are joint height, solder volume, solder pad size, and number of solder pads.

From the *Surface Evolver* calculation to achieve the final joint height of 122 μm after reflow, which is the microlens back focal length, the volume of solder ball has to be $4.39 \times 10^{-6} \text{ cm}^3$. The pad size is numerically calculated to be 190 μm in diameter. Therefore, the solder balls of 8 mil in diameter are used in assembly.

Figure 12 shows the evolution of solder joint through *Surface Evolver*. The number of solder pads is designed to be 8 pads located around the micromirror array to support the weight of entire microlens array chip. The solder pads are fabricated on microlens chip quartz substrate to match the solder pads on micromirror chip. After solder assembly and reflow the two chips are locked in position by cooling down the solder. The alignment occurs automatically during the solder reflow. Figure 13 illustrates the solder self-aligning mechanism.

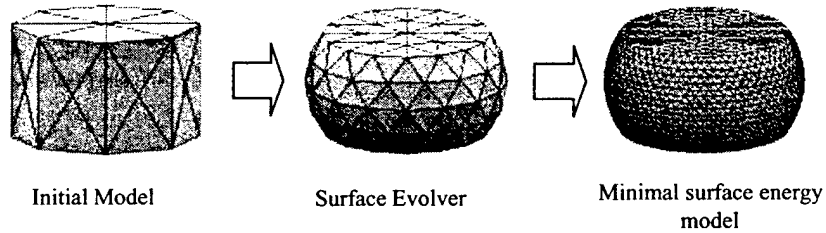


Figure 12 The evolved model of solder joint from *Surface Evolver*.

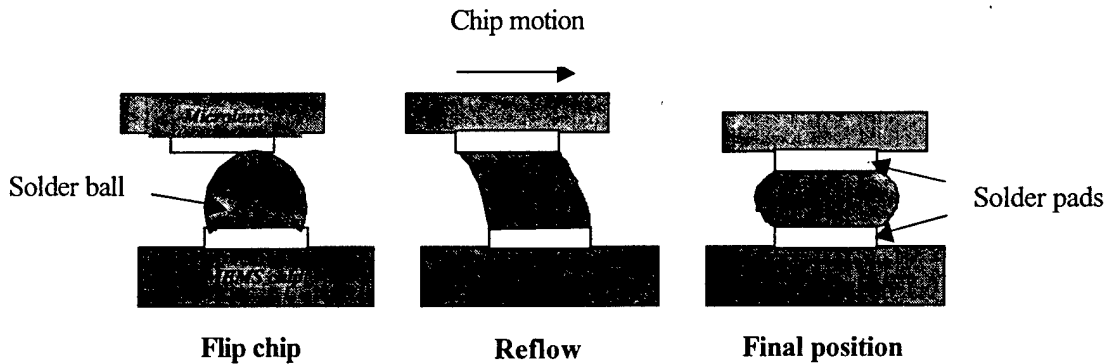


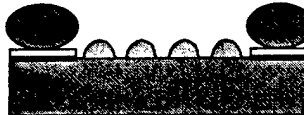
Figure 13. The self-aligning soldering mechanism.

2.2.2 Assembly process

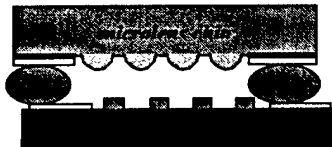
The process of assembly of the microlens array chip on top of the micromirror chip starts by placing the solder onto the gold solder pads of microlens chip. The solder used was eutectic 63Sn/37Pb shaped in spheres of 0.008" in diameter with the diameter tolerance of $\pm 0.001"$. A fluxless soldering process developed for optoelectronics packaging was used in assembly. The solder balls were placed using a vacuum nozzle and micro-positioner. After placement of solder, the microlens chip was placed in a chamber filled with nitrogen and formic acid. The nitrogen gas prevents the solder from oxidizing at high temperature, and at the same time, the formic acid gas removes any oxide that may already exist. The chamber is then heated to 180°C to melt the solder balls and wet the solder pads. The microlens array chip is then flipped and placed on the micromirror array chip. The entire system is reflowed again in the chamber at 180°C. After alignment, the chip is cooled down to lock the assembly. Figure 14 illustrates the assembly process.



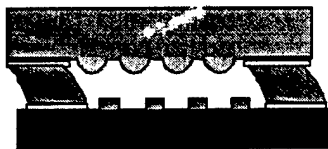
1) Solder pads are fabricated on the microlens array



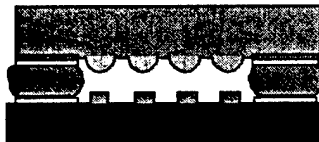
2) Solder balls are placed onto solder pads and reflowed



3) Microlens chip is flipped on micromirror chip



4) Solder is reflowed



5) Assembly is pulled automatically into a well-aligned position and cooled

Figure 14. The polymer lenslet array assembly process.

The lenslet array integrated micromirror chip was packaged into a 24 Pin Grid Array (PGA) using conductive epoxy and electrically connected to packaging by wire bonding. Photographs of the final packaged device are presented in Figure 15. The hybrid lenslet/MEMS arrays thus can be fabricated as rugged, compact optical elements for the beam steering, beam shaping, and aberration correction applications.

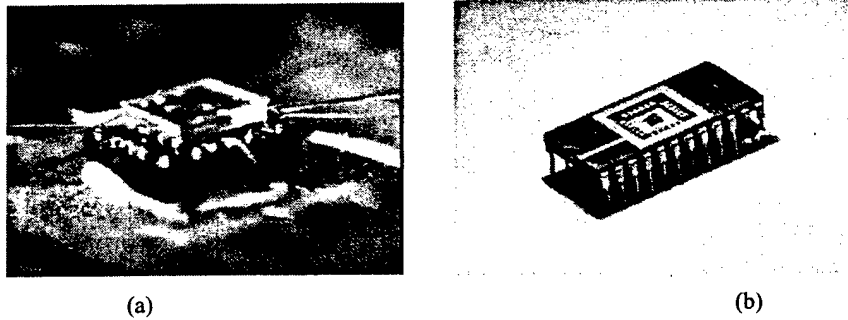


Figure 15. The integrated polymer lenslet array micromirror attached and wire bonded to package (a) and the final device packaged in a 24 PGA (b).

2.3 Experimental Results and Analysis

This section presents the characteristics of our fabricated photo-BCB microlens array, the experimental results from self-aligned soldering flip chip assembly of microlens chip, and the optical performance analysis of LMEM-DM.

2.3.1 Microlens characterization

An interferometric microscope was used as the primary tool to measure the shape and uniformity of lenses. Fringes were observed as the circular rings of increasing width and spacing toward the center of lens as shown in Figure 16(a). Hence the lens's surface is uniform and the shape is spherical. A surface profile measuring system, DEKTAK IID, was used as the secondary tool to measure the surface profile of microlens. Figure 17 shows the measured surface profile of microlens. The spherical surface profile of microlens is clearly shown. The dome height of microlens is $7\ \mu\text{m}$ and the diameter of microlens is $74\ \mu\text{m}$ as expected. The f -number ($f/\#$) of lens is 1.65. In practice, we found that the acceptable photo-BCB lenses can be made with aperture ratios between $f/1$ to $f/3$. A SEM of microlens array successfully formed on a quartz substrate surrounded with solder pads is shown in Figure 16(b).

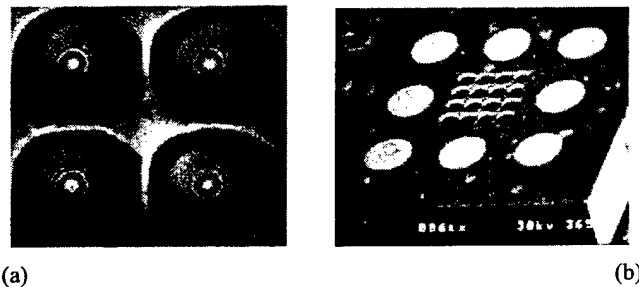


Figure 16. The fringes on lenses detected by interferometric microscope (a) and SEM of microlens array on quartz substrate.

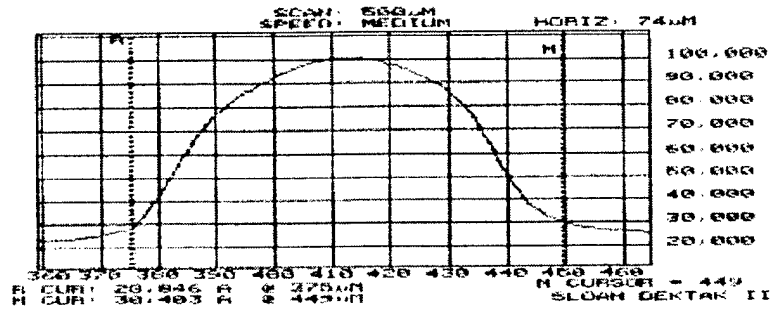


Figure 17. The surface profile of microlens as measured by DEKTAK IID.

2.3.2 Assembly characterization

The photo-BCB microlens array was integrated onto MEMS-based micromirror array and the self-aligned soldering mechanism was successfully applied as the alignment method. The gap between microlens chip and micromirror was measured as $122 \pm 1 \mu\text{m}$ by microscope vertical focusing verification method. The result showed that the *Surface Evolver* solder model was able to accurately predict the solder joint height after thermal reflow. The gap height misalignment is less than 1% of the predicted final gap height. The error occurred due to the variation in solder volume. The solder balls used are manufactured with $\pm 0.001''$ tolerance in diameter. This is a considerable volume variation, so its effect needs to be carefully calculated in the future.

The lateral alignment of microlens chip on micromirror chip was carefully observed during solder's thermal reflow. Figure 18 shows the lateral alignment of microlens chip before and after solder reflow. The success of this solder assembly leads to a novel low-cost batch assembly capability of lenslet arrays with micromirrors.

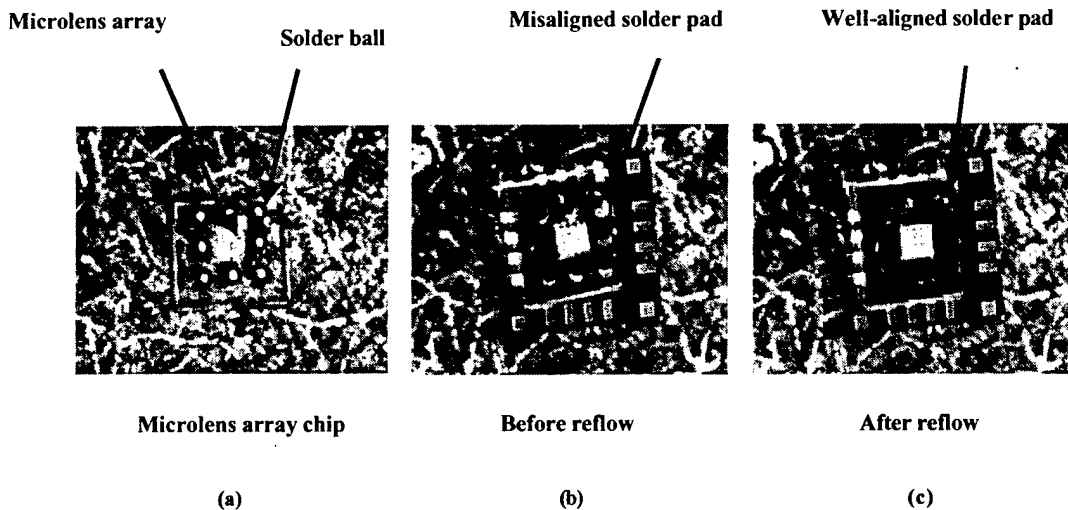


Figure 18. The microlens chip with solder balls before assembly (a) and the lateral alignment of microlens chip before (b) and after solder reflow (c).

2.3.3 Optical characterization

The reflected wavefront off the bare micromirror array (no lenslets) and the LMEM-DM was measured. The far-field diffraction pattern from both cases is shown in Figure 19. The far-field diffraction pattern of LMEM-DM is obviously clearer compared to that of bare micromirror array. The static background interference effect is reduced. In Figure 19(a), the far-field diffraction pattern of bare micromirror consists of the unwanted diffraction pattern located around the central lobe and the blur in the higher order lobes. When the lenslet array is integrated onto the micromirror, the far-field diffraction pattern is significantly improved. The main central and higher order lobes are focused down as round spots. The lenslet array is a two dimensional periodic array of phase modulated circular apertures, so we observe the expected Airy function around the central lobe as shown in Figure 19(b).

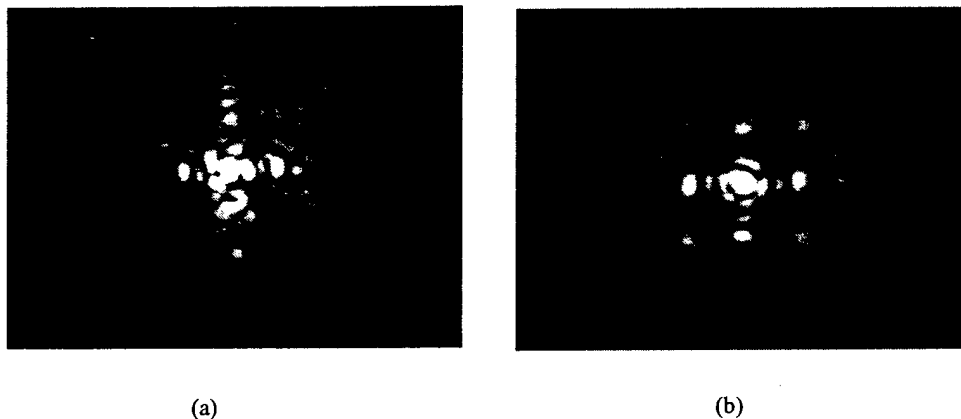


Figure 19. The diffraction pattern in the vicinity of zeroth order of bare micromirror array (a), and of the LMEM-DM with polymer lenslets (b).

2.4. SUMMARY OF POLYMER LENSLET LMEM-DM

The polymer lenslet array has been successfully fabricated with photo-BCB on a quartz substrate and then integrated with MEMS-based micromirror using self-aligned soldering flip chip assembly. The control of gap between the two chips was accomplished using the precise final height of solder balls, as calculated by *Surface Evolver* modeling software. The lateral alignments were achieved accurately by self-aligning mechanism. The use of self-aligning soldering technology to assemble the lenslet array on micromirror helps reduce the overall cost of assembly and increase the yield of LMEM-DM. The use of a lenslet to focus the incoming laser beam onto the reflective surface of micromirror substantially increases optical fill factor of the micromirror array and significantly improves the far-field diffraction.

Published paper:

- A. Tuantranont, V.M. Bright, J.L. Zhang, W. Zhang and Y.C. Lee, "Self-Aligned Assembly of Microlens Arrays with Micromirrors," *SPIE* Vol. 3878, pp. 90-100, 1999.

3. SMART PHASE-ONLY MODULATED MICROMIRROR ARRAY FABRICATED BY STANDARD CMOS PROCESS

Smart, phase-only modulation micromirror arrays have been implemented through a commercial CMOS service. The device is a novel, 2-dimensional array of deflectable micromirrors with integrated CMOS switching circuits and piezoresistive deflection sensors on flexures. The individual mirror pixel is capable of modulating light in the visible to near-infrared spectrum by piston-like movement of a trampoline-type suspended micromirror driven by thermal multi-morph actuators. A flip chip bonding technology is used to integrate the micromirror array with a microlens array to increase the optical fill factor of the hybrid system. Analytical and finite element models verified by experiments were developed to predict and model electro-thermo-mechanical behavior of the micromirror. A 2.5 mrad beam steering angle was successfully demonstrated.

3.1 Introduction

The use of industrial CMOS technology enables the co-integration of mechanical microstructures with integrated circuits on the same chip. Smart MEMS are achieved by integration of digital or analog signal amplifying and processing ICs right next to the MEMS devices. Smart, phase-only micromirror array is a promising integrated microsystem that leads to many applications such as optical beam steering, optical data interconnect, real-time image recognition, optical interferometer, spectroscopy and aberration correction. Large deflection of micromirror is required to be able to modulate light in infrared wavelength. Surface micromachining can be used to fabricate parallel plate structures for electrostatically-driven segmented micromirrors and continuous-membrane deformable micromirrors. However due to a narrow gap between the electrodes in a surface micromachined process, the mirror's deflection is in the range of submicrometer or larger if the structure elevation method is used to increase the gap. Bulk micromachined micromirror is an alternative solution to modulate light at longer wavelengths. In addition to the long travel range, other advantages of our CMOS micromirror include low cost, high yield, mass production, and easy integration of digital or analog electronics in a standard IC process.

The thermal multi-morph actuator, which is a multi-layer structure of metal and polysilicon encapsulated with silicon dioxide is easily fabricated using all the materials available in a standard CMOS process and is used to actuate micromirror. Due to the differences of thermal expansion coefficient (CTE) of the stacked materials comprising the actuator, the beam curls and deflects the attached mirror when a resistive heating from input electrical power is applied. As a thermally-activated mechanical device, the fundamental issues of interest are the steady-state temperature increase and distribution as a result of the electro-thermal heating, and the resulting deflection of the mirror. Many analytical models exist that describe the behavior of bimorph and multi-morph beams; however, the actuator used in our device is not a pure bimorph or multi-morph cantilever beam because its cross section is not uniform along its length, nor are all the important layers in the flexure of the same length. Therefore an electro-thermo-mechanical model was developed to characterize the specific actuator structure of our micromirror. Two steps were taken to model the static deflection of the thermally-actuated micromirror. The first step consisted of extending the existing bimorph-beam theory to take into account the unique geometrical features of the flexures. The second step used finite element analysis to determine the effects of the temperature distribution on mirror deflection. Then, the model was verified by experimental results.

The usefulness of the micromirror device for optical beam steering applications is demonstrated through the 2.5 mrad beam steering angle.

3.2 CMOS Micromirror

The novel 2-dimensional array of deflectable micromirrors was fabricated by the Orbit 2 μm double polysilicon, double metal CMOS process, available through the MOS Implementation Service (MOSIS). The micromirror is designed to modulate light in the visible to near-infrared wavelengths by piston-type movement of micromirror. The individual mirror pixel consists of a $40\ \mu\text{m} \times 40\ \mu\text{m}$ trampoline-type micromirror plate suspended by thermal multi-morph flexures at each corner, as shown in Figure 20(a). The suspended micromirror plate includes stacked aluminum commonly available in standard IC processes. The aluminum shows a high optical reflectivity ($>90\%$) over operation wavelengths. The micromirror plate and multi-morph actuators are coupled with an oxide spring beam. The thermal multi-morph structures consist of polysilicon resistor wires and aluminum layers encapsulated in SiO_2 , as shown in Figure 20(c). Due to the different coefficients of thermal expansion of multi-layer sandwich of different materials, the flexures curl when an ohmic heating from the input electrical power is applied, thus causing piston-type motion of the micromirror plate. The array is anisotropically etched in EDP solution to release the micromirror structure. A pit is formed under the suspended pixel structure, giving high degree of thermal isolation from the surrounding substrate. Piezoresistive deflection sensors, as shown in Figure 20(b), are integrated on flexures of each micromirror to provide feedback control of the position of each micromirror to improve device performance in real-time. Integrated CMOS switching circuit adjacent to each pixel, as shown in Figure 21, works as a switching "AND" gate allowing the current to go into the row and column addressed pixel. The switching circuit allows to address the pixel by 5 V data pulses and operate in digital mode. The multi-morph beam is $72\ \mu\text{m}$ long, $14\ \mu\text{m}$ wide and $4.175\ \mu\text{m}$ thick with $2.8\ \mu\text{m}$ wide and $0.4\ \mu\text{m}$ thick polysilicon heater wire running between aluminum layer and oxide layer to generate heat. The ends of multi-morph actuator beams are coupled to the micromirror plate with the oxide beams ($21\ \mu\text{m}$ long, $7\ \mu\text{m}$ wide and $3\ \mu\text{m}$ thick). After the anisotropic silicon etching has undercut and released the cantilever beams, the beams curled up out of the substrate plane due to internal stresses in their thin structural layers. The etched micromirror plate is thus elevated above the substrate plane by $0.5\ \mu\text{m}$. The flatness of the micromirror is measured using white light interferometric microscope. The peak-to-valley of the unactuated micromirror is $0.22\ \mu\text{m}$ ($\approx \lambda/20$ of maximum operating wavelength).

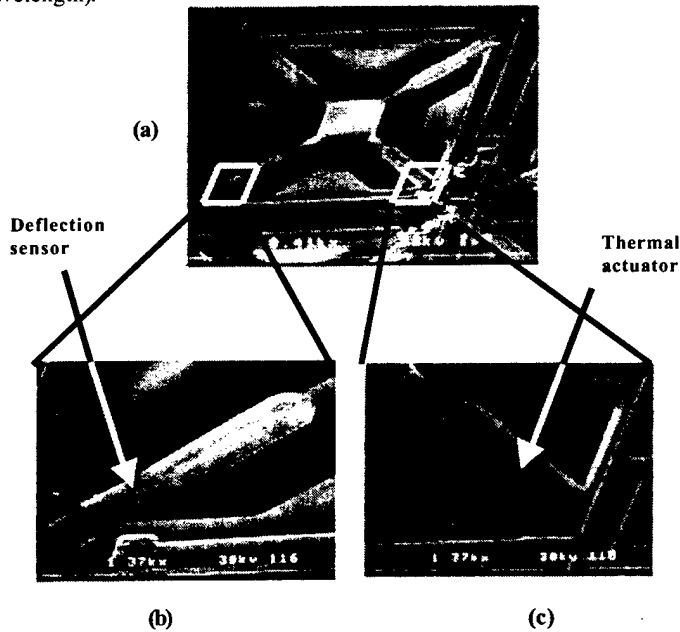


Figure 20. SEM of a pixel of micromirror (a), flexure with embedded resistor for piezoresistive deflection sensor (b), and embedded polysilicon wire heater in the thermal multi-morph actuator (c).

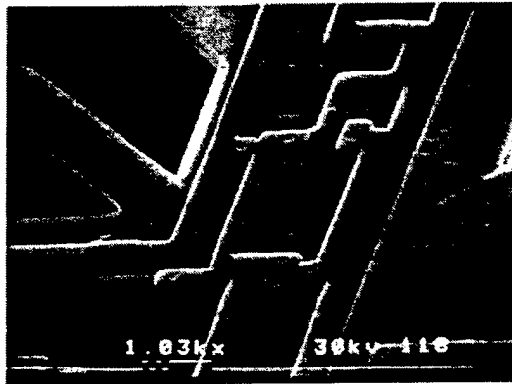


Figure 21. Adjacent, integrated CMOS switching circuit for digital mode operation of the micromirror.

3.3 Finite Element Modeling

An analytical model has been developed to predict the flexure tip deflection [L.A. Liew, A. Tuantranont, V.M. Bright, "Modeling of thermal actuation in a bulk-micromachined CMOS micromirror," *Microelectronics Journal*, vol. 31, pp. 791-801, 2000]. This is sufficient for a first order approximation but not if more detailed analysis is required. Particularly, the analytical model does not predict any induced mirror plate deformations that may arise due to the thermally induced bending of the actuators. A finite element model was thus constructed to perform a more detailed analysis of the micromirror behavior.

A simulation of the micromirror was conducted with a commercially available finite element analysis tool (MARC). The model consists of stacked layers of solid elements with thicknesses that correspond to the actual structural layers fabricated. The simulation consists of an electro-thermal analysis to obtain the temperature distribution resulting from an input electric power. This is then coupled to a mechanical analysis in which the temperature distribution is used to determine deflections resulting from the thermal expansion mismatch in a multi-morph structure.

3.3.1 Electro-thermal analysis

An input voltage was applied to the polysilicon heating resistors of micromirror model, which correspond to the two thermal actuators. The other two of the four flexures contain piezoresistors for measuring mirror deflection. Heat transfer paths considered were the thermal conduction to the substrate and to the surrounding air. Both the air and substrate were assumed to remain at room temperature. Convection and radiation through air were not considered because of their negligible effect. Only the steady state condition was considered in the analysis, corresponding to a static deflection of micromirror. Figure 22 shows the vertical temperature profile through the stacked layers of the thermal actuator at various positions along the length of the actuator. The maximum temperature is in the metal layer, thus it contributes the most to actuation. The temperature in the polysilicon and oxide layers decrease along the length of the actuator. Near the base of the actuator, the temperature of the metal and the polysilicon is close, but the difference increases along the length of the flexure.

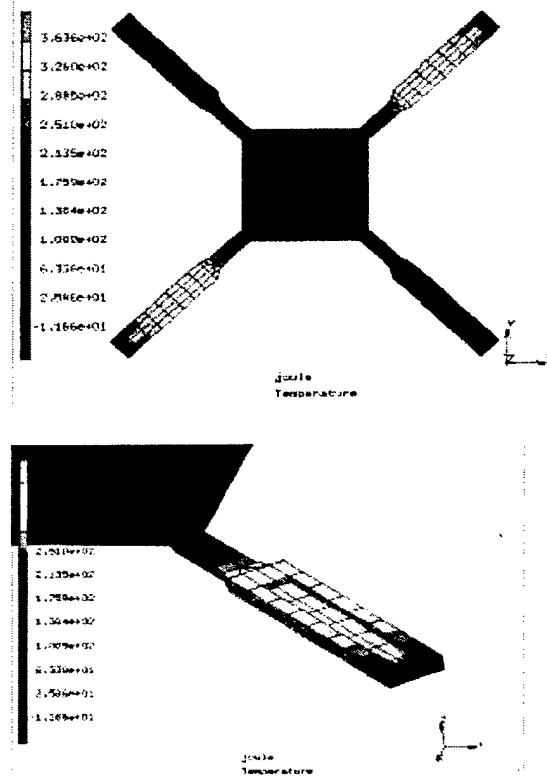


Figure 22. FEM results showing the vertical temperature profile through the stacked layers comprising the thermal actuator for an applied voltage of 7 volts.

3.3.2 Thermal-mechanical analysis

The temperature distribution resulting from the electro-thermal analysis was used as an input condition for the thermal-mechanical analysis. Figure 23 shows the finite element structural model of the micromirror when it is deflecting. Boundary condition is used to fix the location of the beam's base. Figure 24 shows the results from the analytical model, finite element models and experimental results of mirror deflection versus applied voltage.

3.4 Micromirror Characterization

3.4.1. Static analysis

Micromirror deflection

Measurements were taken to determine the maximum possible deflection of the micromirror, and the deflection of micromirror versus applied power. Deflection of micromirror was measured over a range of input power by white light interferometric microscope. Measurements were taken on the center of

micromirror. Figure 25 shows the experimentally determined mirror deflection versus applied power. The mirror deflection depends linearly on the drive power with maximum power of 150 mW per pixel at $2 \mu\text{m}$ deflection with nonlinear effect near zero due to the buckling of heated beam. There is no observed tilting of the actuated micromirror from both the simulation and the experimental results.

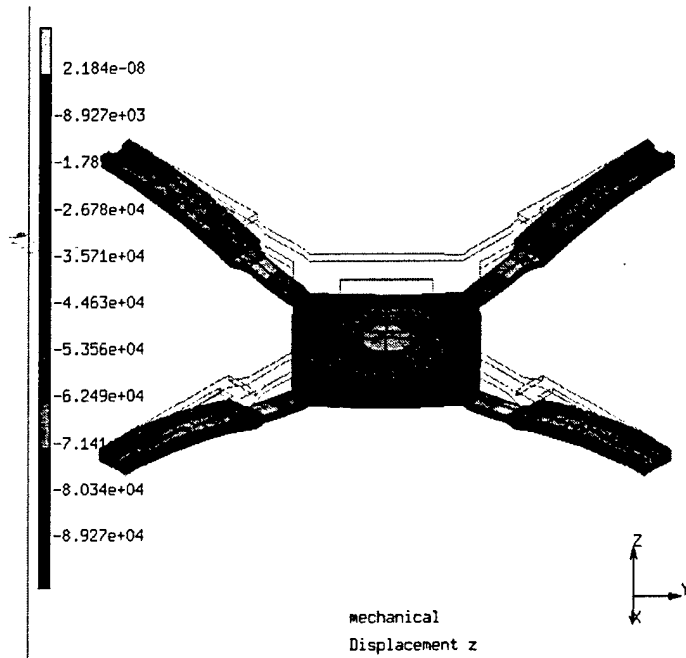


Figure 23. FEM result showing the deflection distribution of micromirror.

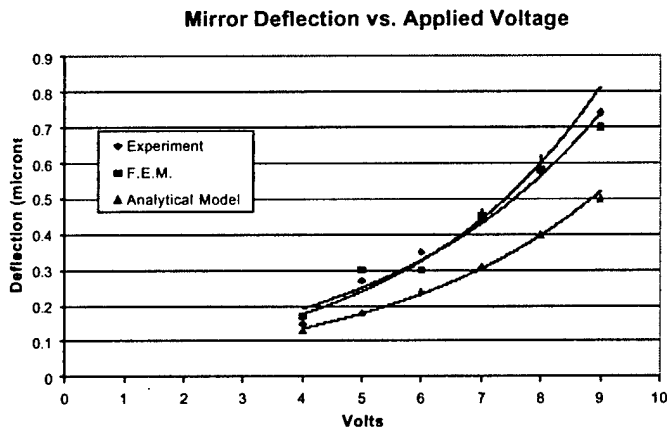


Figure 24. Mirror deflections obtained from the analytical model, the finite element model, and experimental results in voltage range of 4 to 10 Volts.

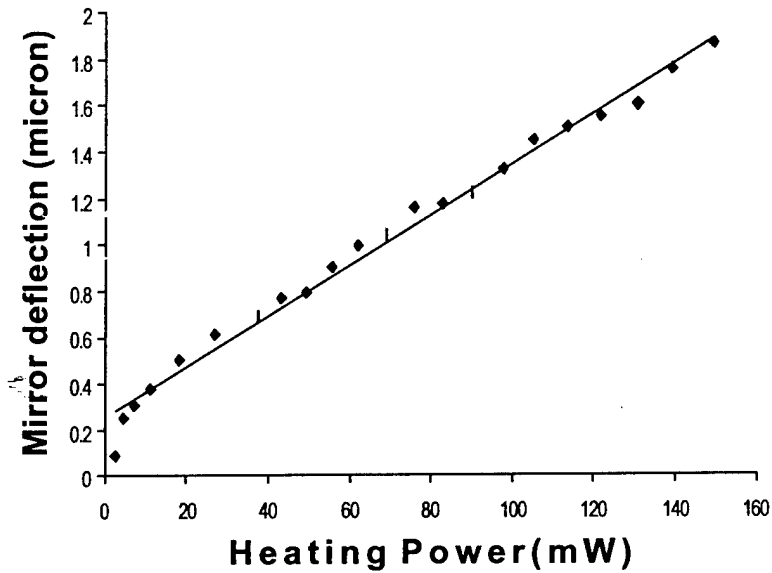


Figure 25. Micromirror deflection versus heating power.

Piezoresistive detection

Deflection of the micromirror is detected with two piezoresistors embedded in the opposing beams. The position of the piezoresistors is at the clamped edges of the beams, where the mechanical stress is highest. The measured change in resistance in a single piezoresistor related to the mirror deflection as a linear relation is shown in Figure 26. Through Figure 26, a known relationship may be established to provide the feedback signal for real-time control of micromirror.

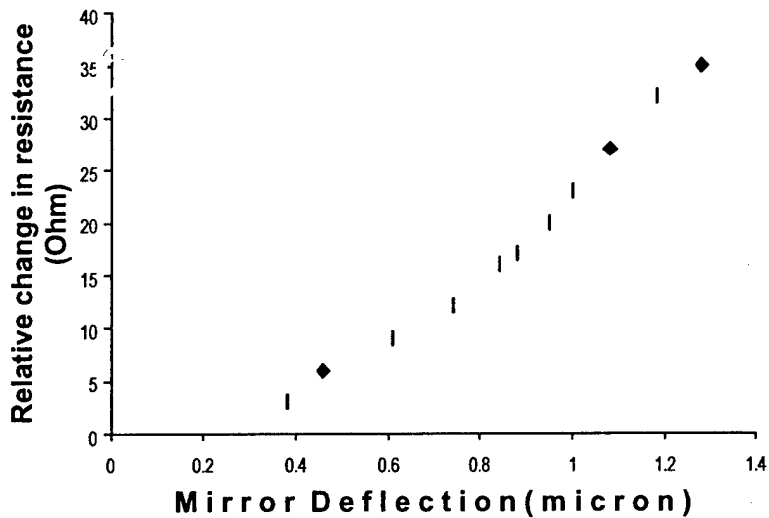


Figure 26. Mirror deflection versus relative change in resistance of a single piezoresistor.

3.4.2 Dynamic characterization

Dynamic measurements were taken to determine the maximum operating frequency of the micromirror. Laser interferometer was setup and used to determine the time required to heat and cool the multi-morph beams. The micromirror was driven by a 4 Hz, 5 volt peak input signal. Figure 27 shows the driving input signal and output signal from photodetector. The upper trace indicates the square wave input and the lower trace indicates the interference fringe movement. The onset of heating or cooling of the beam occurs immediately after applied voltage changes. After the multi-morph beam reaches a steady state temperature, the micromirror stops moving and interference pattern stops changing. The heat and cool times for the multi-morph beam are 3 ms, but the encountered force of the oxide beam spring during micromirror actuation results in an increase of mirror total response time (heating time=7 ms) to 10 ms. The maximum operating frequency of 100 Hz is achieved. Below this frequency, the multi-morph will completely heat and cool following the drive signal. Above this maximum frequency, multi-morph beam will not have adequate time to heat and cool and so will not completely deflect in either direction.

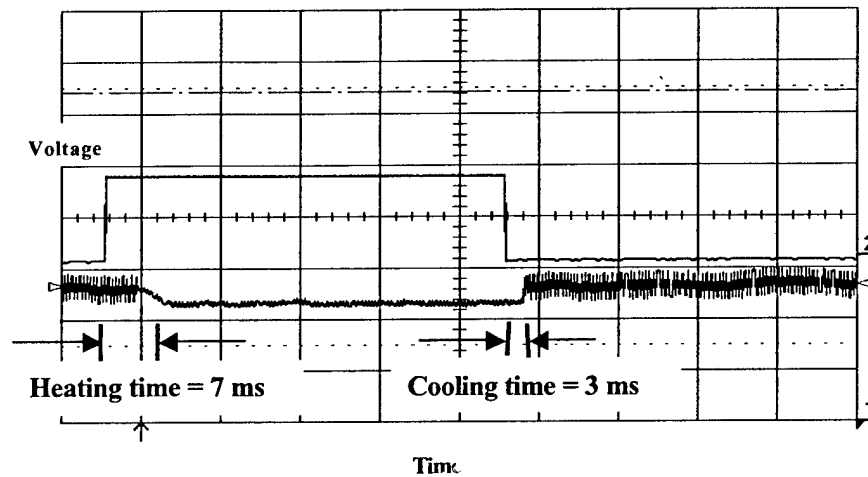


Figure 27. Experimental result showing input square wave to a CMOS mirror and output interferometer data.

3.5 Micromirror/Microlens Integration

Using the refractive lenslet array to focus the incident light beam onto only the reflective surface of the mirror is one way to greatly improve the effective optical fill factor with corresponding decrease in static background interference effect. The CMOS micromirror was designed specifically for use with an available commercial refractive lenslet array from Nippon Sheet Glass Company. Each microlens has a circular shape 250 μm in diameter. The 250 μm center-to-center spacing of the lens array matches with the center-to-center spacing of the micromirror array. The back focal length of the microlens is 560 μm . This lenslet array can provide approximately 90% light transmission at visible wavelengths. Hybrid flip-chip assembly is applied to integrate the lenslet array on top of the micromirror array. Two glass spacers of 1.925 mm thickness and 1 mm x 14 mm were attached to the 16.5 mm x 14 mm quartz window with 20 μm thick UV curable epoxy. The lenslet array was flipped and attached to the quartz window by UV curable epoxy. The quartz window with lenslet array was flip chip attached to the micromirror package and pre-cured under UV light. The alignment was then adjusted manually in the X and Y position. Afterward, the lenslet array integrated micromirror was

investigated under interferometric microscope. Fringe patterns observed by the interferometric microscope were used to correct possible tilt alignment of the lenslet array. The focal point of lenslet was aligned on the center of the micromirror, afterward the epoxy was cured firmly. From observation, the gap between the microlens and micromirror was controlled by the spacers accurately and equals to the focal length of the microlens (error <2% in X-Y-Z position). Figure 28 shows the close-up view of the flip-chip integrated lenslet array on top of the 4x4 micromirror array. The final device was packaged in a 40 pin dual-in-line (DIP) package.

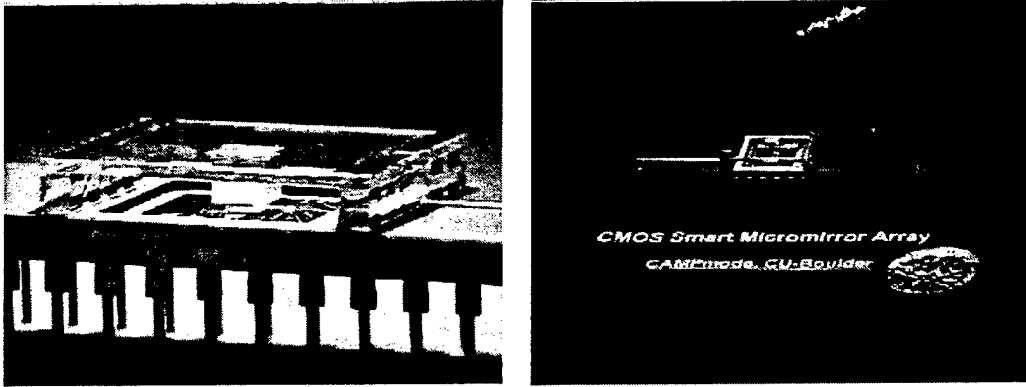


Figure 28. The lenslet array flip-chip integrated on top of the CMOS micromirror array using glass spacers for gap control, and the final device packaged in a 40 pins DIP package.

3.6 Phased Array Beam Steering

The optical experimental setup of Figure 7 was used to measure the far-field diffraction pattern of the lenslet integrated CMOS micromirror tested for beam steering or aberration correction. In one dimension an optical phased array of n elements, with uniform phase shift spacing between elements from 0 to 2π radians, steers a beam to an angle $\theta_s = \lambda/nL$, where L is the spacing of the elements (in this case the lenslet dimension), and λ is the operating wavelength. Beam steering of 2.5 mrad from boresight (Figure 29 and Figure 30) is implemented by a stepped linear ramp pattern across the columns of the micromirror. Steering angle measurements show excellent agreement (within 1% error) with one-dimensional beam steering theory.

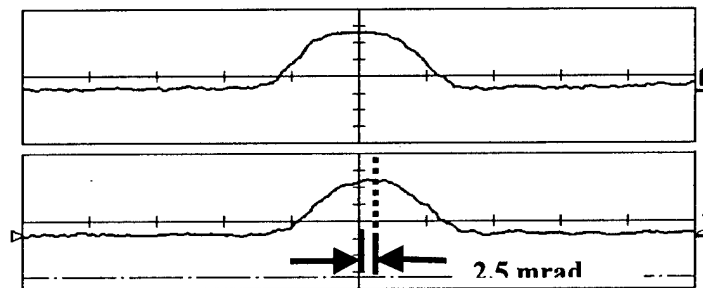


Figure 29. The beam profiles of unsteered (trace A) and steered beam (trace 1).

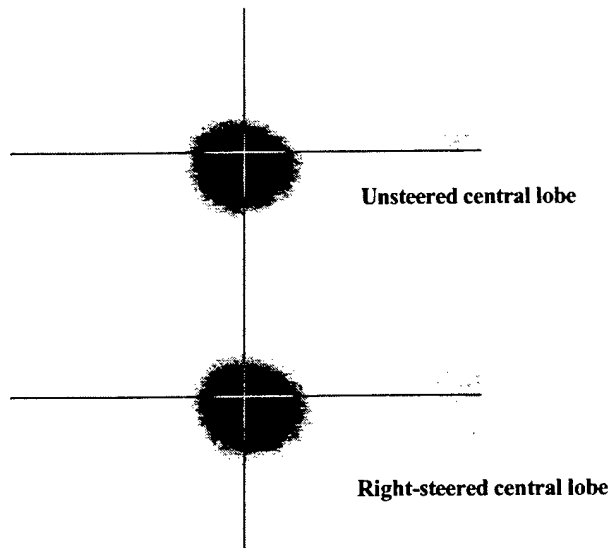


Figure 30. Central maximum beam steering for a 16 element micromirror array.

3.7 SUMMARY

The phase-only CMOS micromirror array has been successfully fabricated by a standard CMOS process. The micromirror is actuated by thermal multi-morph actuators and deflection is detected by piezoresistors. The CMOS switching circuit is integrated adjacent to the individual pixel to address current to the pixel and allow the device to operate in digital mode. A glass lenslet array is flip-chip hybrid integrated on top of the micromirror to increase the optical fill factor of the system. The hybrid mirror/lenslet array can modulate the light in visible to near infrared wavelengths (400 nm – 4 μ m wavelength). The device was used to demonstrate optical beam steering ability up to 2.5 mrad.

Published papers:

- A. Tuantranont, V.M. Bright, L.A. Liew, W. Zhang, and Y.C. Lee, "Smart Phase-Only Micromirror Array Fabricated by Standard CMOS Process," IEEE MEMS 2000 Proc., pp. 455-460, 2000.
- L.A. Liew, A. Tuantranont, V.M. Bright, W.Zhang, and Y.C.Lee, "Thermal Analysis of CMOS Micromirror's Multi-morph Actuators," Microelectronics Journal, Vol. 31, pp. 791-801, 2000.
- A. Tuantranont, V.M. Bright, L.A. Liew, W. Zhang, and Y.C. Lee, "Phase-Only Micromirror Array Fabricated by Standard CMOS Process," to appear in Sensors and Actuators Journal.

4. MEMS-CONTROLLABLE MICROLENS ARRAY

Novel, 2-dimensional MEMS-controllable microlens array has been integrated with a Vertical-Cavity-Surface-Emitting-Laser (VCSEL) array using flip-chip assembly. The MEMS/VCSEL hybrid system is built as an efficient and reliable smart pixel array for board-to-board or chip-to-chip optical interconnects in digital systems. Theory including geometrical and Fourier transform analysis and beam steering experiments were developed. By translating polymer microlens, fabricated on a MEMS X-Y movable plate, using electro-

thermal actuators, a beam steering angle of 70 milliradian is achieved. VCSEL beam steering was successfully demonstrated in our MEMS/VCSEL hybrid system to collimate and steer laser beam for a precision alignment in a 2-dimensional free-space optical interconnect.

4.1 Introduction

Free-space optical interconnection is attractive for several applications including telecommunication switching networks and fine-grained parallel processing/computers. Currently optical interconnects are used for data communication over long and medium distances in wide area networks (WANs). However over short distances inside computer systems or clusters of electronic networks, board-to-board or chip-to-chip multi-GHz bandwidth optical interconnects are required to replace electrical interconnects in the near future. This replacement is necessary due to problems with signal integrity and crosstalk at high frequency in electrical interconnects. The advantages of free-space holographic interconnects include direct interconnects between boards, arbitrary interconnection patterns, multiple fan-outs, and channel isolation and increased bandwidth, thus avoiding the interconnection bandwidth bottleneck of systems with strictly in-plane electronic interconnects. Furthermore, the cost of free-space interconnects has been reduced substantially with the advancement of vertical-cavity surface-emitting lasers (VCSELs). However alignment challenges are inevitable in optical interconnect systems. Mechanical vibrations or thermal expansion can cause misalignment. We thus developed an enhanced alignment approach for free-space interconnects without a demand for tighter assembly tolerances using a MEMS-controllable microlens array. Figure 31 shows the use of MEMS-controllable microlens array to enhance alignment in board-to-board optical interconnect. The microlens collimates an incident VCSEL beam and the microlens actuators steer the beam to a predefined position on a hologram array by laterally translating the microlens.

Several groups have recently described efforts to steer laser beam using decentered microlens techniques. These approaches require light-weight and small travel of the microlens components to achieve agile beam steering. Despite the number of papers on decentered microlens beam steering, all of them seem to require a large space for array of actuators such as comb-drive actuators or scratch drive actuators (SDA) to laterally translate microlens. Moreover, none of them has operated at a VCSEL wavelength of 830 nm because the MEMS devices need to be fabricated on a silicon substrate, which is not transparent at this wavelength. The device in our approach contains a dense array of individually controllable microlenses, allowing for operation with a VCSEL array. The design, theory, modeling, fabrication, MEMS/VCSEL integration, and experimental results of beam steering are presented.

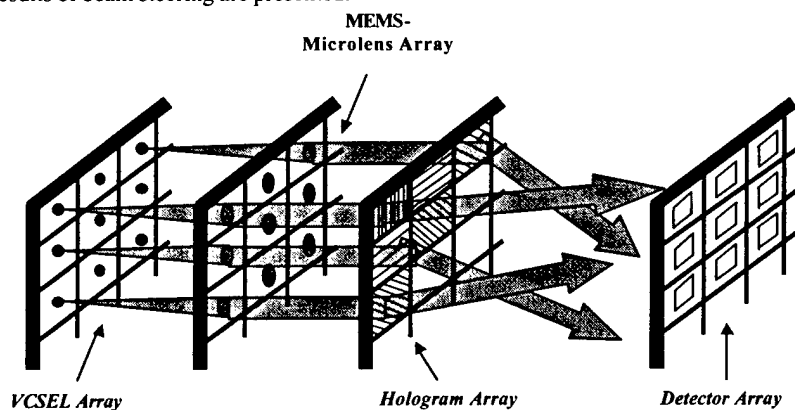


Figure 31. MEMS-controllable microlens array for enhanced alignment in a 2-D board-to-board optical interconnect.

4.2 MEMS-Controllable Microlens Array Device Description

The 2-dimensional MEMS-controllable microlens array was fabricated through the commercially available surface micromachining technology (Multi-User MEMS Process - MUMPs). BCB electronic resin, a photo-sensitive polymer, was used in our own process to fabricate micro semi-spherical polymer lenses on MEMS. Each 120 μm focal length microlens was fabricated directly on a MEMS X-Y movable plate with a 30 μm circular aperture as shown in Figure 32. The microlens was modeled as a thin paraxial lens. The focal length of the microlens is set by controlling the initial thickness of the photo-BCB layer and the diameter of the lens, which are defined by photolithography. The photo-BCB thickness required for a given radius of curvature for the lens was calculated by equating the volume of spherical portion representing the final lens shape to the volume of a cylinder representing the photo-BCB column before reflow. Transmission of microlens is more than 95% at operating wavelength (850 nm). The lens profile deviates less than 5% from an ideal spherical lens. Since only a small fraction of the lens surface is used to refract light, the effects of spherical aberration and steering-angle-dependent off-axis wavefront aberration are minimized.

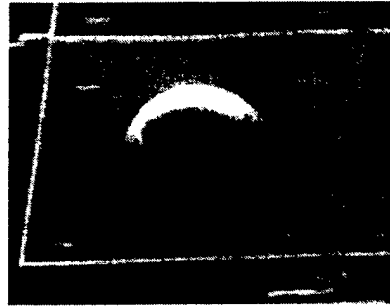


Figure 32. Polymer microlens fabricated on a polysilicon MEMS movable plate.

Two arrays of electro-thermal actuators are coupled with the 80 μm \times 80 μm polysilicon movable plate to translate the microlens in X-Y plane. The microlens array is located at a focal plane in front of the VCSEL array and collimates the incident VCSEL beams. 'U'-shaped lateral electro-thermal actuators or 'heatuators' used to drive central plate in a lateral motion consist of a single-material connected narrow arm and wider arm. Current is passed through the polysilicon actuator, and the higher current density in the narrower 'hot' arm causes it to heat and expand more than the wider 'cold' arm. The arms are joined at the free end, which constrains the actuator tip to move laterally in an arcing motion towards the cold arm side. The tips of the actuators are coupled to the central plate by long thin flexures on opposite sides of the plate. Left actuator in Figure 33 pulls the plate while the right actuator pushes the plate at the same time. By push/pull mechanism of actuators, the motion of the plate is linearly proportional to the consumed power. The mechanical crosstalk in X and Y directions is minimized by using long thin flexures. The concept of decentered microlens for beam steering is shown in Figure 34.

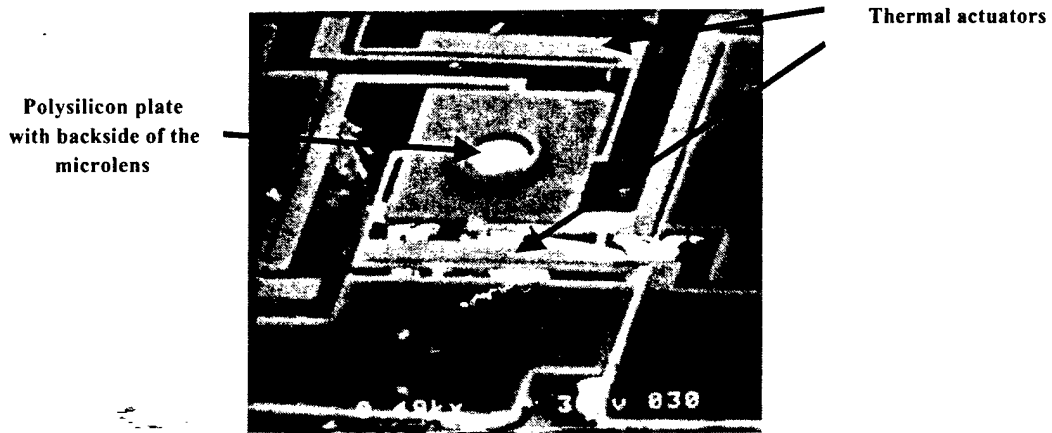


Figure 33. SEM of electro-thermal actuators attached to a suspended polysilicon plate.

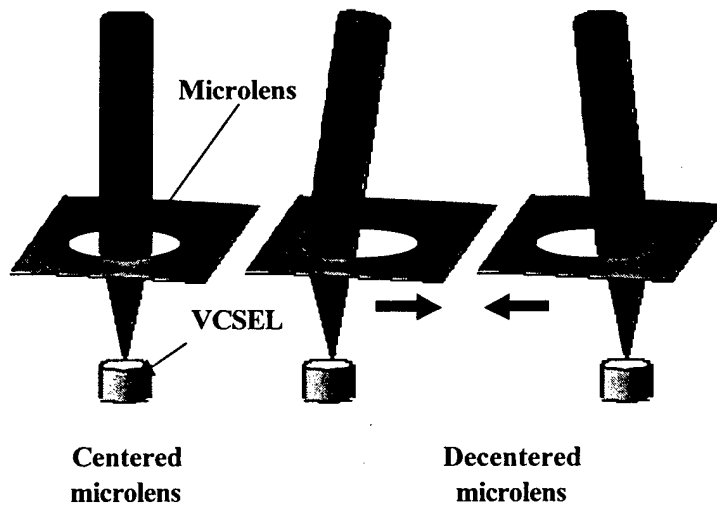


Figure 34. The decentered microlens concept of MEMS-controllable microlens array.

4.3. Modeling and Finite Element Analysis

A simulation of the MEMS-controllable microlens was conducted with ABAQUS, which is a commercially available finite element analysis tool. The model consists of an electro-thermal analysis to obtain the temperature distribution resulting from a simulated input power to electro-thermal actuators. This is then coupled to mechanical analysis in which the temperature distribution is used to determine deflections resulting from thermal expansion in the arms of actuators. The finite element simulation of the temperature distribution in actuators and movement of the plate are shown in Figure 35.

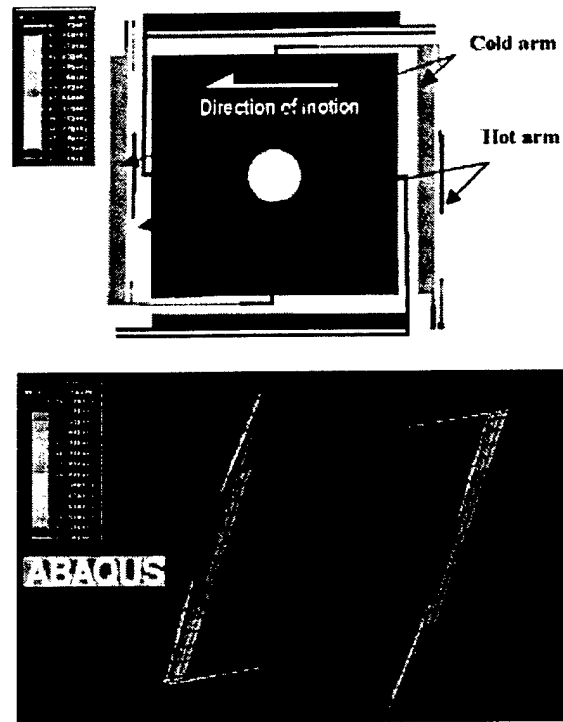


Figure 35. Finite element simulation of the thermal distribution and movement of electro-thermal actuators.

4.4 MEMS Flip-Chip Transfer and Integration

The procedures for flip-chip transfer of MEMS to a non-silicon substrate (in this case quartz substrate) need two post-processing steps. First, the MEMS structures are fabricated at a commercial foundry as shown in Figure 36(a), where a MEMS device is attached to the silicon substrate only by the oxide encasing it. The target substrate is patterned with gold interconnects and bonding pads designed to receive the MEMS structures, as shown in Figure 36(b). Then, in the second step shown in Figure 36(c), the two chips are bonded together by thermosonic bonding. Finally, the bonded structure is subjected to a hydrofluoric acid (HF) rinse, as shown in Figure 36(d), to free the MEMS structure and remove the silicon substrate.

The MEMS-structures were designed and patterned in the first releasable polysilicon layer of the MUMPs process. The photo-BCB microlenses are patterned and fabricated on polysilicon plates by our own process. The plates and actuators are built upside-down on top of sacrificial oxide so that the bonding pads fabricated on MEMS are matched with bonding pads on quartz target substrate. The quartz receiving substrate was patterned with gold wires and bonding pads for MEMS flip-chip bonding and wire bonding. A masked layer of photoresist is used to protect the quartz and gold interconnects when the assembly is released in HF. Gold bumps of 70 μm height are placed on pads and used to bond and electrically connect the MEMS structure and the wiring substrate. The MEMS-controllable microlens array is then flipped and bonded with the wiring quartz substrate using thermosonic bonding. The final step in the process is to release the bonded device in a HF bath and remove the silicon substrate. The final device after flip-chip transfer to a quartz substrate is shown in Figure 37.

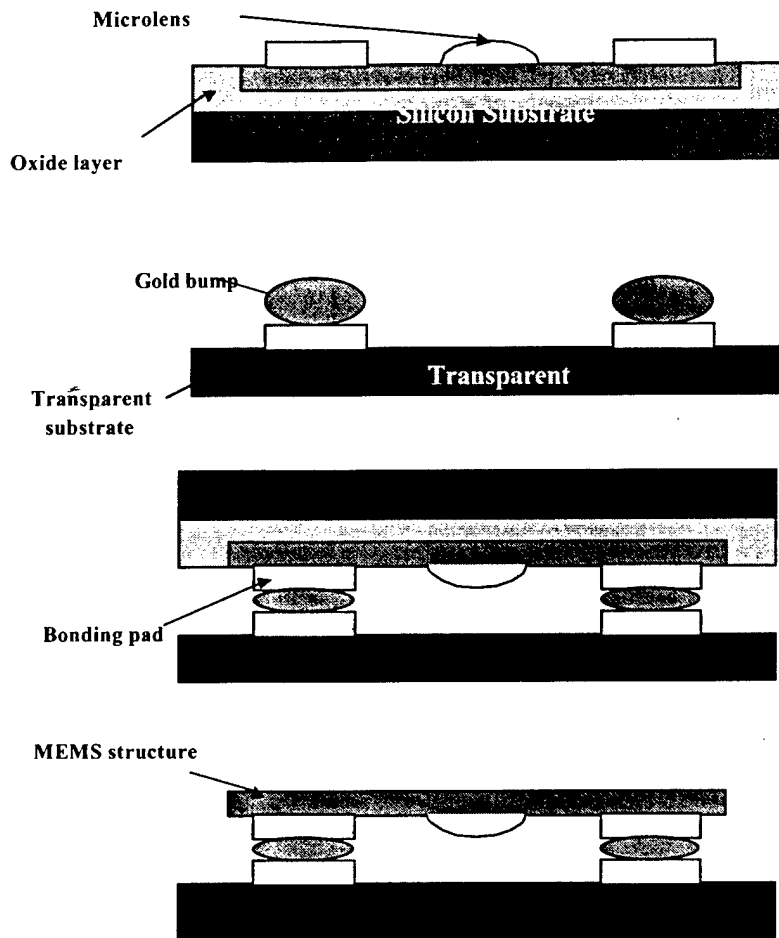


Figure 36. Flip-chip assembly of MEMS to a non-silicon substrate.

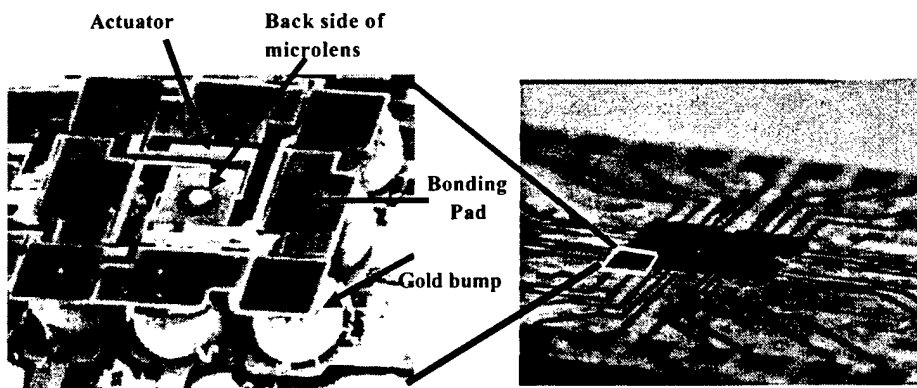


Figure 37. SEM images of the flip-chip assembled MEMS-controllable microlens 4x4 array on a quartz substrate.

4.5 MEMS/VCSEL Integration

The VCSEL array consists of an 8×8 array of top-emitting VCSELs on a 250 μm pitch. Molecular Beam Epitaxy (MBE) was used to grow the VCSEL structure on a GaAs substrate. The VCSEL structure consists of two distributed Bragg reflector (DBR) mirrors surrounding a single GaAs quantum well, and is ion implanted for current confinement in the active region. The VCSEL operates at approximately 830 nm with a bandwidth of 0.2 nm and a 2 nm wavelength variation across the array. A Gaussian beam with a (e^{-2}) half-angle of 0.135 radians (2 μm in waist) is emitted from the top surface. The threshold current is 1.5 mA. The VCSEL array is flip-chip bonded on a quartz substrate using thermosonic bonding. 90 μm square bonding pads for attachment of the flip-chip bonds are evenly interspersed amongst the VCSELs. Each pad is located a distance of 125 μm (center-to-center) from its associated VCSEL. The bonding process uses gold or gold-tin alloy, which is applied to the contacts. The thermosonic bonding method utilizes transverse ultrasonic energy to soften the bonding materials and uses low temperature (<500 K on the substrate only) and an assembly force ≈ 0.3 N/bump. A vision assisted, computer controlled placement and assembly machine is used for bonding. Substrate and chip are each centered in separate viewing cameras which allow the relative location of the components to be determined. The substrate is held in a computer controlled translation stage, and the chip is held in a chuck, which is attached to the ultrasonic transducer. The translation stage is used to move the substrate into the aligned position under the chip, and both chips are bonded together. Figure 38 shows a flip-chip assembled VCSEL array on a quartz substrate with CMOS driving circuit.

Both flip-chip MEMS and flip-chip VCSEL chips are bonded together using UV curable epoxy and aligned under a microscope to correct the lateral misalignment. The optical interferometric microscope is also used to correct the tilt of the final assembly. Then the final assembly is flip-chip bonded to a ceramic fan-out wiring substrate. The MEMS/VCSEL assembly is then packaged in a 144 ceramic pin grid array (PGA). The schematic diagram of the final assembly is illustrated in Figure 39.

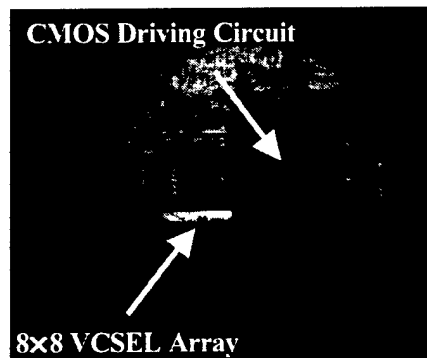


Figure 38. Flip-chip assembled 8×8 VCSEL array on a quartz substrate.

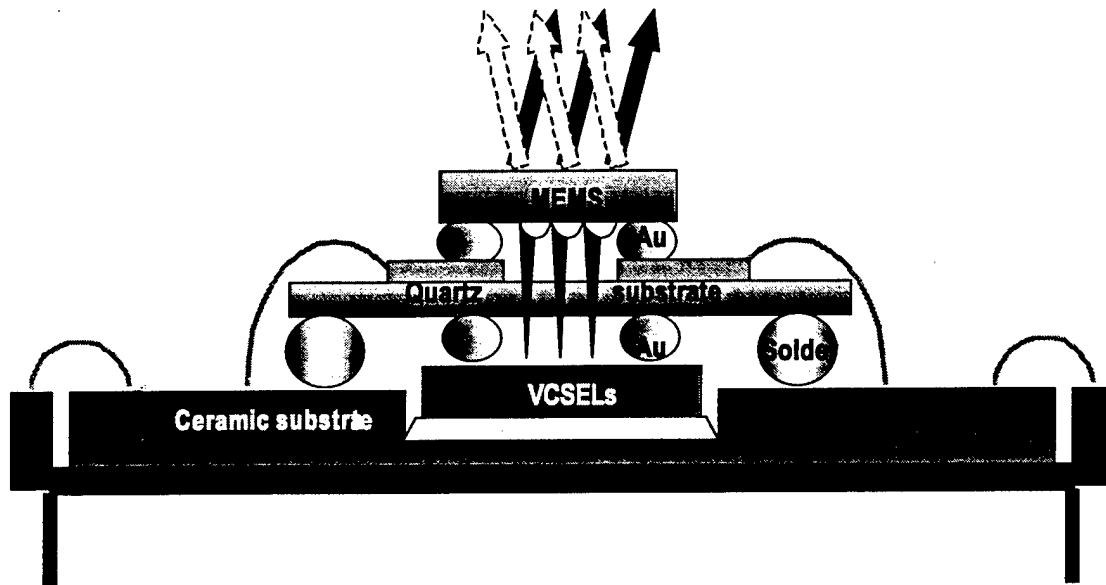


Figure 39. Schematic diagram of the final MEMS/VCSEL assembly and package.

4.6 Beam Steering Experiment and Results

CAD program for optical system design, OSLO, was used to simulate the beam steering of the VCSEL beam. The MEMS-controllable microlens array chip was then actively aligned with the VCSEL array chip. First, a decentered keplerian telescope is used to achieve a collimated beam steering. The controllable microlens is placed at its focal length f_M in front of the focal plane of the lens f_L . The microlens then collimates and steers beam to the desired directions by translating in X-Y plane (refer to Figure 40).

Consequently, the telescope optics, which consist of positive lens ($f_1 = 100$ mm) and negative lens ($f_2 = -50$ mm) are used to magnify the steering angle by the ratio of $f_1 / f_2 = 2$. CCD camera was used to detect the deflection of the beams in the far field plane. The 2-dimensional beam steering is successfully demonstrated as shown in Figure 41.

The maximum beam steering of 70 milliradian (≈ 4 degrees) is implemented by translating the microlens by one-half of the lenslet diameter as shown in Figure 42, which is adequate for enhancing optical alignment in free-space optical interconnects. The measured steering angles well agree with the theoretical calculation. Measurement verified insertion loss of the system is less than 2 dB. The system was demonstrated up to a rate of 1 kHz of operation frequency, result of the low inertia and small travel of the microlens components.

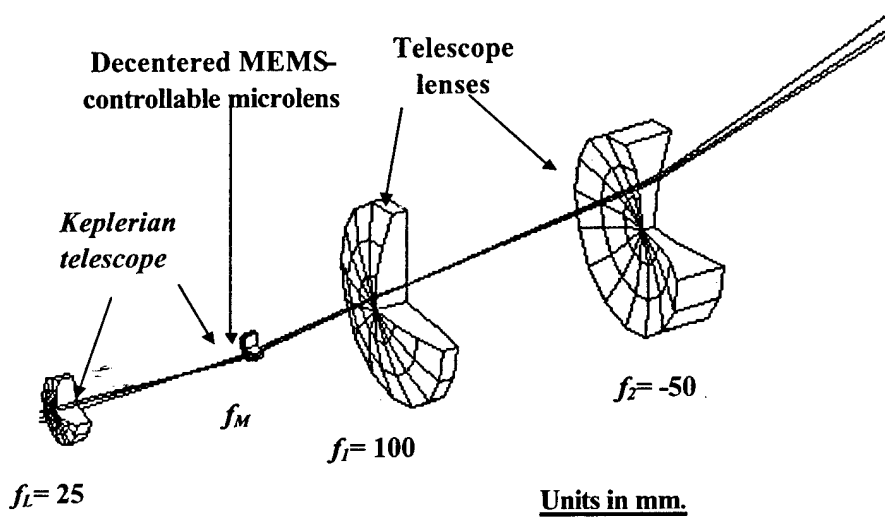


Figure 40. Optical experimental setup for beam steering demonstration.

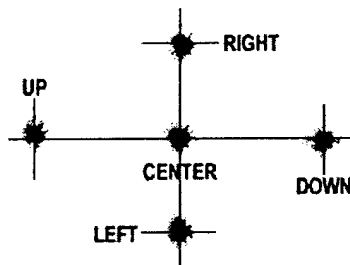


Figure 41. The 2-dimensional beam steering demonstration.

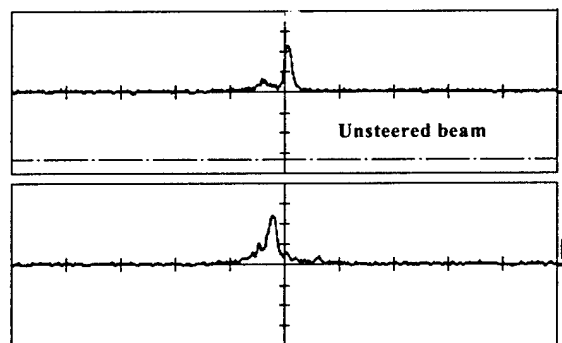


Figure 42. The maximum beam steering angle of 70 milliradians.

4.7 SUMMARY

Novel, 2-dimensional MEMS-controllable microlens array has been integrated with a Vertical-Cavity-Surface-Emitting-Laser (VCSEL) array. By translating polymer microlens fabricated on a MEMS X-Y movable plate using electro-thermal actuators, the 2-dimensional beam steering is demonstrated and the maximum beam steering of 70 milliradian is achieved. VCSEL beam steering was successfully demonstrated in our MEMS/VCSEL hybrid system to collimate and steer laser beam for a precision alignment in a 2-dimensional free-space optical interconnect system.

Published papers:

- A. Tuantranont, V.M. Bright, J. L. Zhang, W. Zhang, J. Neff, and Y.C. Lee, "MEMS-Controllable Microlens Array for Beam Steering and Precision Alignment in Optical Interconnect Systems," Technical digest of Solid-state Sensors and Actuators Workshop' 2000, pp. 101-104, Hilton Head Island, South Carolina, USA.
- A. Tuantranont, V.M. Bright, J. Zhang, W. Zhang, J. Neff, and Y.C. Lee, "Optical Beam Steering Using MEMS-Controllable Microlens Array," to appear in Sensors and Actuators Journal.

5. BULK-ETCHED SURFACE MICROMACHINED AND FLIP-CHIP INTEGRATED MICROMIRROR ARRAY

The 2-dimensional phase-only micromirror array is a promising microsystem that leads to many applications such as optical beam steering, optical data interconnects, real-time image recognition, optical spectroscopy, and aberration correction. Large deflection of micromirror is required to be able to modulate light in infrared wavelength. In previous works on piston micromirrors, surface micromachining was used to fabricate parallel plate structures with a narrow gap between the mirror and underlying address electrode, that is not adequate to modulate light in longer wavelength than in visible spectrum. We have developed a novel technique that combines the surface and bulk micromachining to implement an infrared micromirror array.

5.1 Device Configuration and Fabrication

The novel 2-dimensional array of deflectable mirrors begins with fabrication of the actuators (Figure 43) through MUMPS. MUMPS is a three-layer surface micromachining polysilicon process. The individual MEMS actuator pixel consists of a $40\mu\text{m}\times 40\mu\text{m}$ trampoline-type polysilicon plate suspended by thermal bimorph actuators at each corner, as shown in Figure 44. The central polysilicon plate and bimorph actuators are coupled with a spring oxide beam. The thermal bimorph actuator consists of a polysilicon resistor encapsulated in SiO_2 and a gold layer. Due to the different coefficients of thermal expansion of multi-layer sandwich of different materials, the actuator flexures curl when an ohmic heating from input electrical power is applied, thus causing piston-type motion of the central polysilicon plate. A flip-chip transfer technique is used to integrate $248\mu\text{m}\times 248\mu\text{m}$ polysilicon micromirror plates with $2\mu\text{m}$ spacing between mirrors on top of the actuator array; the micromirror plates are also fabricated through MUMPS but on a separate chip. The assembled results in a MEMS mirror array of very high optical fill factor (99%). Gold bumps were used as the posts and thermosonic bonding was used to bond the actuator array and polysilicon mirror plates together. The bonded structure was then annealed to relax the stress in gold bumps and released in a hydrofluoric acid rinse to remove the silicon substrate and free the micromirror structures. The array is anisotropically etched in EDP solution to form pyramidal pits under the suspended pixel structures, giving high degree of thermal isolation from the surrounding substrate. The assembly

configuration is illustrated in Figure 45. An array of micromirrors that have been flip-chip transferred onto the actuator array is shown in Figure 46 (one mirror in the lower right corner is removed to display actuator structure underneath).

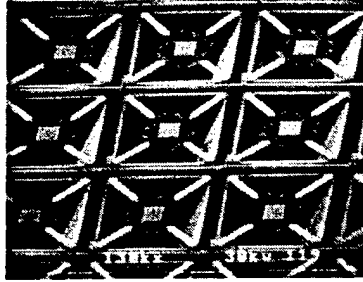


Figure 43. A portion of 2-dimensional actuator array for use with piston-type micromirrors.

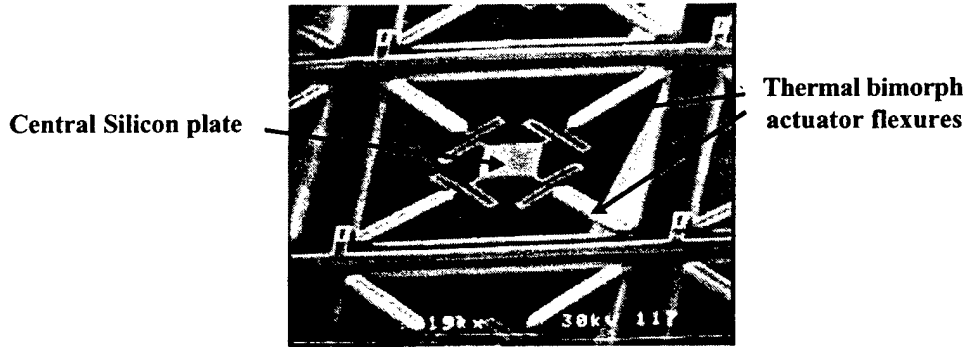


Figure 44. Trampoline-type actuator configuration.

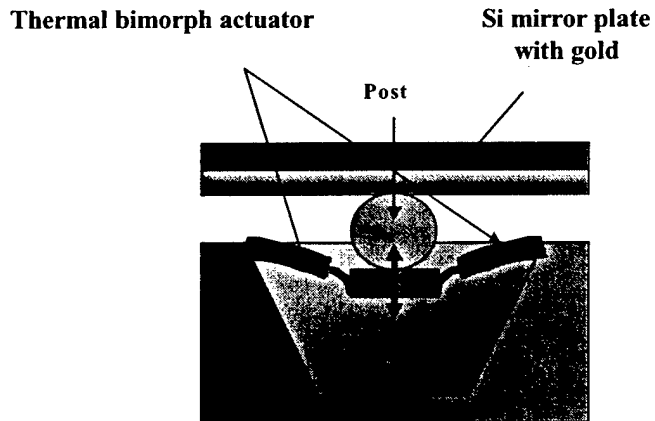


Figure 45. Illustration of the assembly configuration.

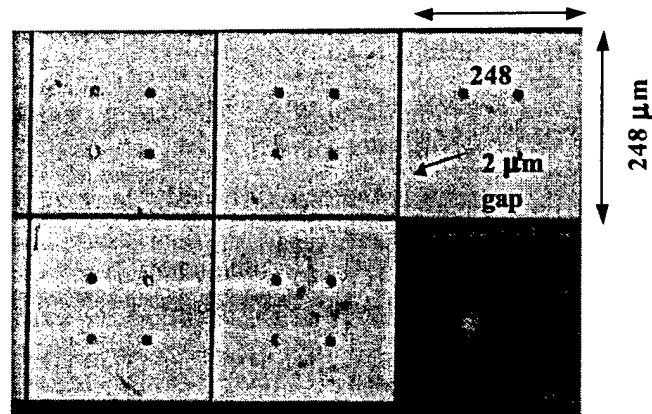


Figure 46. Array of $248\ \mu\text{m} \times 248\ \mu\text{m}$ mirrors with $2\ \mu\text{m}$ gap flip-chip transferred onto actuator array.

5.2 Micromirror Characterization

Measurements were taken to determine the relationship between the deflection of micromirror and actuator applied heating power, as shown in Figure 47. Deflection of micromirror was measured by a white light interferometer microscope. The mirror deflection depends linearly on the actuator drive power with the maximum deflection of $4\ \mu\text{m}$, which means that the operating wavelength of this device is in the range of $4\ \text{nm}$ to $8\ \mu\text{m}$. Dynamic measurements using laser interferometer setup were taken to determine the maximum operating frequency of the micromirrors. The maximum operating frequency of $100\ \text{Hz}$ is achieved with the complete heat and cool cycle following the drive signal. The surface profile of micromirror was measured by interferometric microscope as shown in Figure 48. The measured peak to valley of each micromirror is less than $0.4\ \mu\text{m}$, which is approximately $\lambda/20$ of the maximum operating wavelength. Thus this device can be implemented in adaptive optics applications.

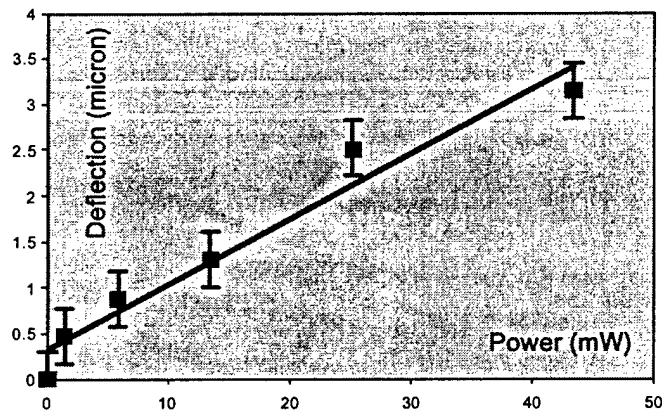


Figure 47. Micromirror deflection versus actuator applied power.

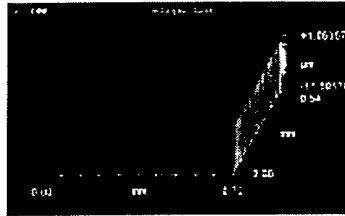


Figure 48. Surface profile of assembled micromirrors.

5.3 SUMMARY

2-dimensional phase-only micromirror arrays were implemented through a novel bulk-etched surface micromachining process. Flip-chip transfer was used to assemble micromirrors with MEMS actuators. The assembled large-stroke micromirrors can modulate light in visible to infrared spectrum.

Published paper:

- A. Tuantranont, L.A. Liew, V.M. Bright, J.L. Zhang, W. Zhang, and Y.C. Lee, "Bulk-Etched Surface Micromachined and Flip-Chip Integrated Micromirror Array for Infrared Applications," Proc. IEEE/LEOS Optical MEMS 2000, pp. 71-72, 2000.

6. THERMAL-ELECTRICAL-MECHANICAL COUPLED ANALYSIS OF MICROMIRROR UNDER HIGH ENERGY ILLUMINATION

6.1 Thermal Analysis

When micromirror array is used for laser modulation, it is subjected to high heat fluxes. The reliability and performance of the mirrors are related to their operating temperature, therefore thermal management is a key consideration in the design of micromirror for high power applications. High temperature can ablate micromirror surfaces, melt supporting flexures, or distort reflective surfaces and reduce the optical efficiency of the system. Previous thermal testing showed the effects of baking micromirror at different temperatures [D. Burns and V. M. Bright, Vol.1, pp. 335-338, *Transducers '97*, 1997]. All devices baked at temperatures of 250°C or more resulted in visible damage to the gold reflective region (Figure 49). After baking a device at 250 °C for 1 hour, mirror reflectivity at a laser wavelength of 632.8nm dropped from initial value 91.5% to 67.9%. Micromirror reflectivity continued to decrease when the device temperature increased as shown in Figure 50. Above 325°C the gold layer is no longer planar, which caused significant phase distortion in the reflected light. Figure 51 shows the linear relationship of incident laser power and temperature of gold. If the incident optical power is very high, the micromirror can suffer structural damage (Figure 52).

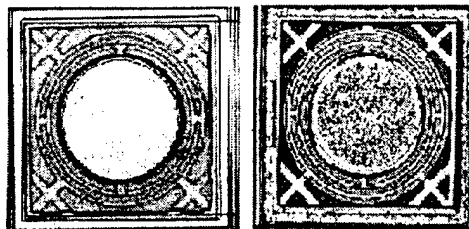


Figure 49. Effects of thermal stress on gold covered micromirrors [D. Burns and V. M. Bright, Vol.1, pp. 335-338, *Transducers '97*, 1997].

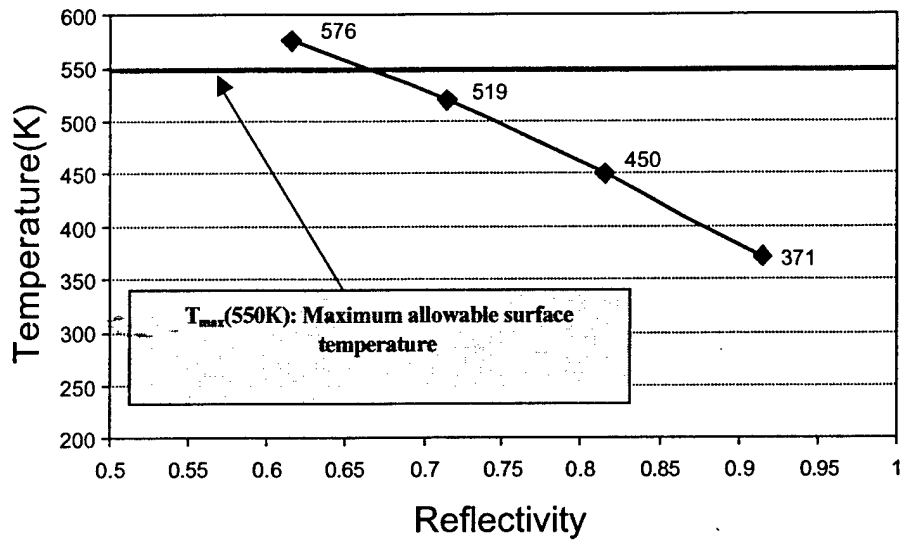


Figure 50. Effect on gold surface reflectivity with increase in temperature.

(high gas pressure P=760 Torr, Nitrogen)

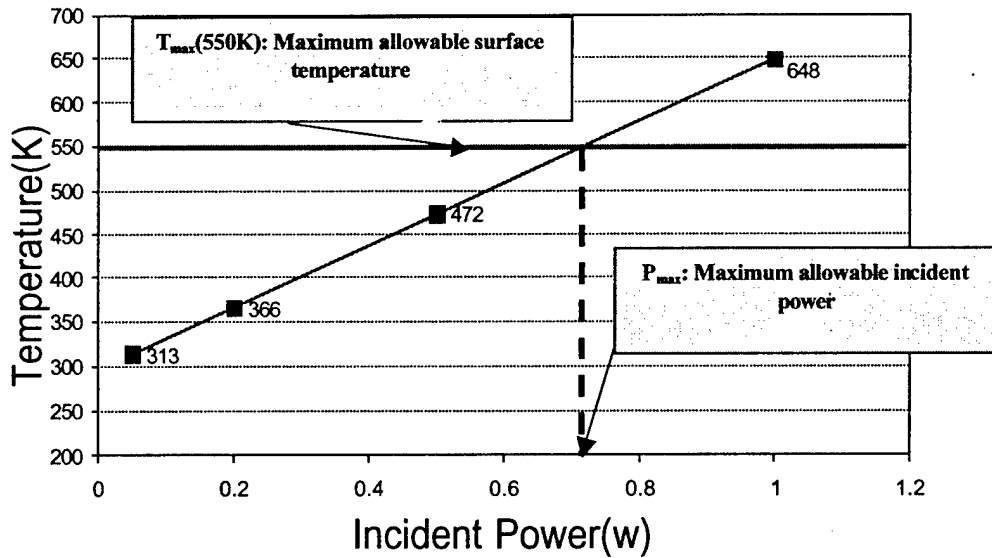


Figure 51. Gold surface temperature versus incident laser power.

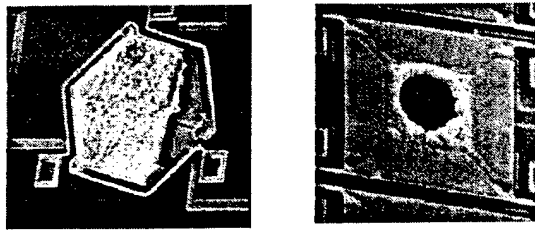


Figure 52. Two micromirrors damaged by excessive laser energy. (a) 12.65 mW and (b) 9.35 mW optical power continuous for 3 seconds.

[D. Burns and V. M. Bright, Vol.1, pp. 335-338, *Transducers '97*, 1997]

6.1.1 Micromirror configuration

Figure 53 shows the layout of our original micromirror design used to test the power handling capability. Figure 54 shows the cross section view of the micromirror.

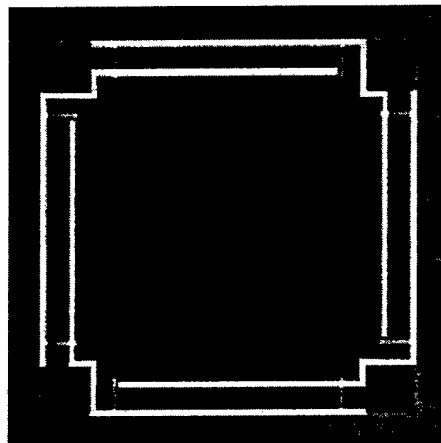


Figure 53. Top view of micromirror construction.

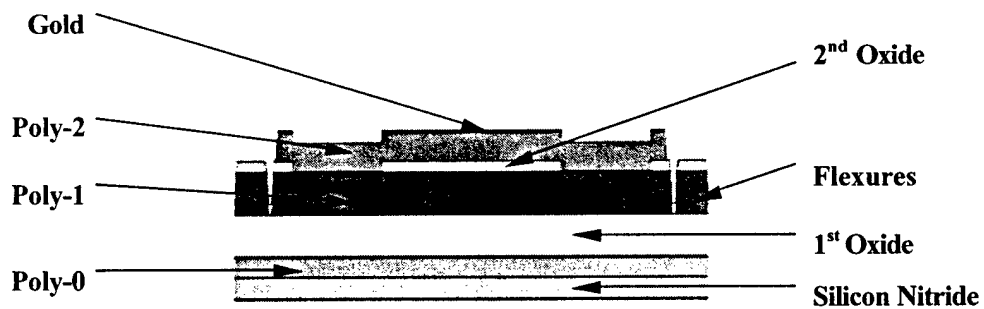


Figure 54. Cross section view of micromirror.

Micromirrors used in our systems were fabricated through Multi-User MEMS Process (MUMPS). MUMPS offer three patternable layers of polysilicon and two sacrificial layers of phosphosilicate glass on a base layer of silicon nitride. A top layer of gold is used as the reflective surface. During the process, silicon nitride is applied first, then the films are deposited on the silicon wafer substrate with the same order of the entries as in Table 3. Table 3 shows the layer thickness for each of the films used in MUMPS. The gold is evaporated on to the device after all other layers have been deposited by low-pressure chemical vapor deposition. The polysilicon layers and the substrate are highly doped with phosphorous (approximately 10^{20} atoms cm^{-3}) to decrease electrical resistance. After fabrication, MEMS devices are released by removing sacrificial glass layers in buffered hydrofluoric acid.

Table 3. MUMPs Structural and Sacrificial Layers.

Layer Name	Nominal thickness (μm)
Nitride(silicon nitride)	0.6
Poly-0(bottom polysilicon layer)	0.5
1 st Oxide(sacrificial layer-phosphosilicate glass)	2.0
Poly-1(middle polysilicon layer)	2.0
2 nd Oxide(sacrificial layer-phosphosilicate glass)	0.75
Poly-2(top polysilicon layer)	1.5
Gold	0.5

6.1.2 Thermal dissipation

Thermal dissipation paths are shown in Figure 55. There are two main paths through which thermal energy is dissipated. One is conduction from gold to substrate and flexures through Poly2, Poly1 and gas gap. Another is surface radiation of gold, poly2 and poly1.

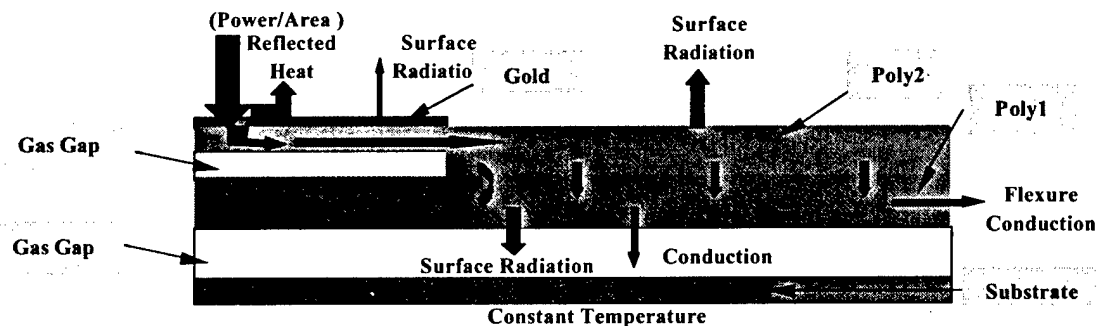


Figure 55. Thermal dissipation paths.

(1) Absorbed power

Assume that only the gold region of the micromirror is illuminated. The absorbed optical power is proportional to the incident power. The absorbed power P_a can be calculated by the following equation as a function of the incident power P :

$$P_a = [1 - R_g(\lambda)]P \quad (1)$$

$R_g(\lambda)$ is the reflectivity of gold, which is a function of the wavelength of the source. Then the heat flux applied on the gold surface can be calculated by:

$$D_{flux} = \frac{P_a}{A} \quad (2)$$

where A is the surface area illuminated by laser beam.

(2) Surface radiation

Micromirrors are usually hermetically sealed in chip carriers to prevent dust and moisture contamination. External forced gas convection is usually not practical. Because of the small scale of the micromirrors, free convection can be neglected. So the thermal dissipation mechanism for surfaces is radiation, including gold and Poly2 radiation to the ambient surrounding gas and Poly1 radiation to the substrate.

Thermal power dissipated by radiation P_r can be given by:

$$P_r = \epsilon\sigma S(T^4 - T_s^4) \quad (3)$$

ϵ is the emissivity of the material, σ is Boltzman's constant, S is the surface area of the material, T is the temperature of the material, and T_s is the temperature of the substrate.

(3) Thermal conduction through surrounding gas

Thermal conduction through the surrounding gas is dependent both on the composition and pressure of gas. For different levels of pressure, thermal conductivity of gas can be calculated by:

$$K_p = \frac{K_g \rho}{\rho_0} \quad (4)$$

K_g is the thermal conductivity of the surrounding gas at a reference pressure ρ_0 , K_p is the thermal conductivity of the surrounding gas at the pressure ρ .

The gas gap between Poly1 and the substrate is very thin ($h=2.0\mu\text{m}$), which is much less than the distance between the mirror and the micromirror package. Thermal conduction through the surrounding gas to the micromirror package is more than two orders of magnitude less than thermal conduction through gas gap to the substrate. So it can be neglected with only a minimal impact on the model's accuracy at low pressure.

At the interface between gas and substrate, a constant temperature is applied as boundary condition, because the substrate is assumed at the temperature equal to the ambient temperature. In fact, when the pressure of the surrounding gas is at 1 atm or above, thermal conduction through gas gap to the substrate will become the dominant heat dissipation path. Substrate cannot be considered at ambient temperature, the

thermal mechanism of whole assembly should be investigated. Convection should also be considered under this condition.

6.2 Modeling Analysis

6.2.1 Gas pressure dependent critical thermal paths

Configuration of thermal analysis is shown in Figure 56(a). Most of incident power is reflected by the micromirror surface. But absorbed power is dissipated by three paths: surface radiation, heat conduction through flexures and heat conduction through gas gap as shown in Figure 56(b).

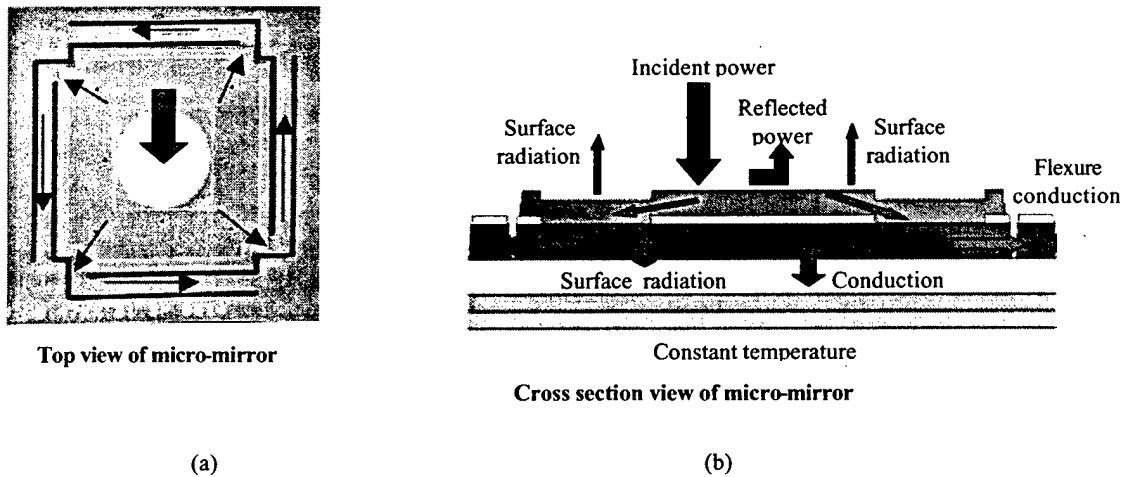


Figure 56. Configuration of thermal analysis and thermal paths.

A finite element model of micromirrors was established and used to investigate thermal mechanism between laser and micromirror. Finite element model of micromirror using ABAQUS is shown in Figure 57. The results of the model indicate that the dominant dissipation mechanism of thermal energy is the flexure conduction for low gas pressure and gas gap conduction for high gas pressure as shown in Figure 58 and 59.

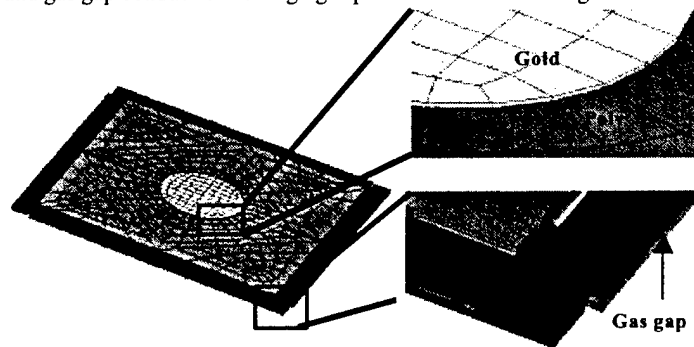
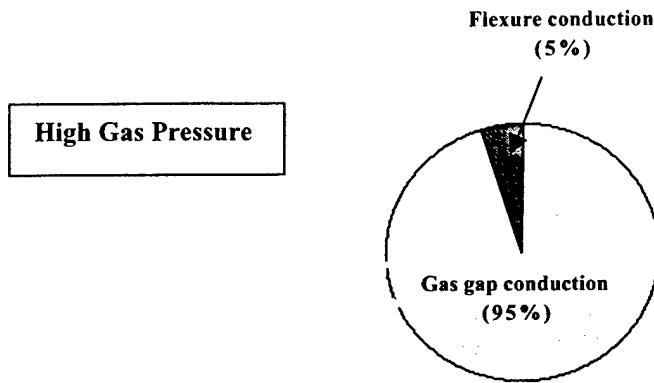
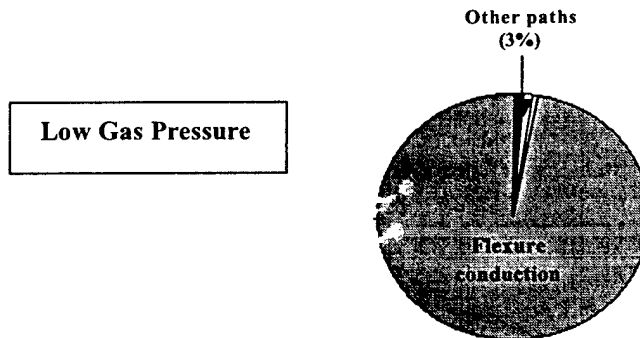


Figure 57. ABAQUS Finite element model of the micromirrors.



Gold surface radiation	Poly2 radiation	Poly1 radiation	Gas gap conduction	Flexure conduction
0.00558 mW (<0.01%)	0.0141 mW (<0.1%)	0.0158 mW (<0.1%)	80.0 mW (95%)	4.2 mW (5%)

Figure 58. Gas gap conduction is the critical thermal path for high gas pressure (Absorbed power:85 mW, $T_{max}=606$ K, $P=760$ Torr).



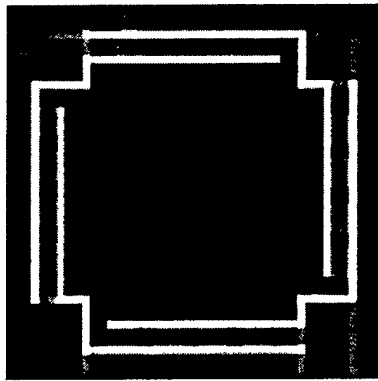
Gold surface radiation	Poly2 radiation	Poly1 radiation	Gas gap conduction	Flexure conduction
0.00765 mW (<0.02%)	0.0385 mW (1.0%)	0.04 mW (1.0%)	0.0289 mW (1.0%)	4.2 mW (97%)

Figure 59. Flexure conduction is the critical thermal path for low gas pressure (Absorbed power:4.25 mW, $T_{max}=640$ K, $P=0.02$ Torr).

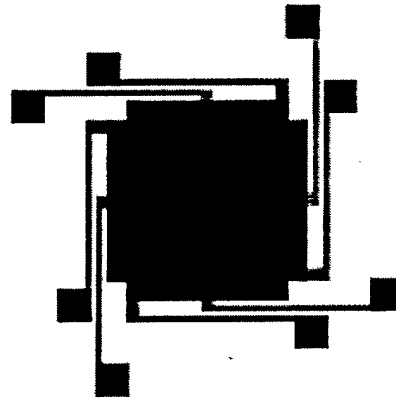
6.2.2 Design improvement

The thermal model established provides us with an insight into the thermal issues for the MEMS-based micro-mirrors. The model is a useful tool to design micro-mirrors for reliable spatial light modulators. If the surrounding gas pressure is very small, flexure design becomes very important because most of the absorbed heat is dissipated by mirror flexures. Geometry of flexures can be designed in order to enhance flexure conduction. If the surrounding gas pressure is at 1 atm or above, most of the absorbed heat is dissipated by gas gap conduction between top electrode and substrate.

In order to get a higher micromirror response frequency, low pressure surrounding gas is required. However, when the surrounding gas pressure is low (less than 0.02 Torr), thermal conduction through flexures is the critical thermal path. One of solutions to reduce the mirror surface temperature is to increase the width of the flexures. But when the width of flexures is increased, spring constant of flexures is unavoidably increased and the flexures become stiffer. Thus more operating voltage is needed. Changing the flexure design for better heat transfer without affecting electrical-mechanical performance of micromirrors is a challenge. One solution to overcome this challenge is to reduce surface temperature and thermal resistance of the flexures by using segmented gold deposited on flexure as shown in Figure 60(a). Changing flexure distribution is another solution to reduce the mirror surface temperature by increasing the number of the flexures as shown in Figure 60(b). Figure 61 shows the SEM pictures of original and improved designs as discussed.

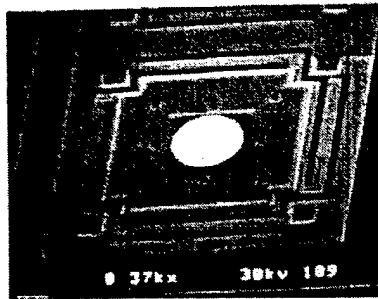


(a)

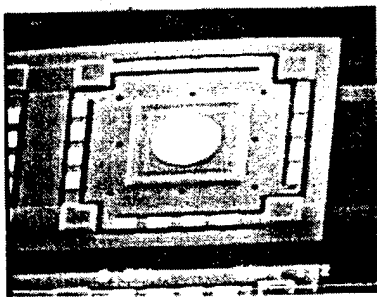


(b)

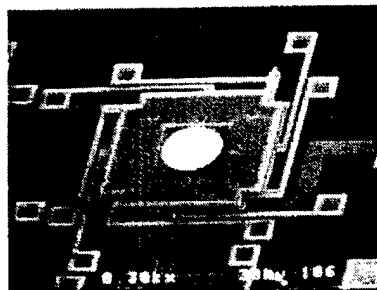
Figure 60. The improved mirror design by segmented coated gold on flexures (a), and by increasing the number of flexures (b).



(a)



(b)



(c)

Figure 61. SEM pictures of original (a) and improved designs (b) and (c).

A commercial available finite element simulation tool, MEMCAD, by Microcosm Technology was used to model and simulate the thermal distribution of both improved mirror designs. Figures 62 and 63 show the solid models of improved micromirror design using segmented gold on flexures and improved micromirror design using increased number of flexures.

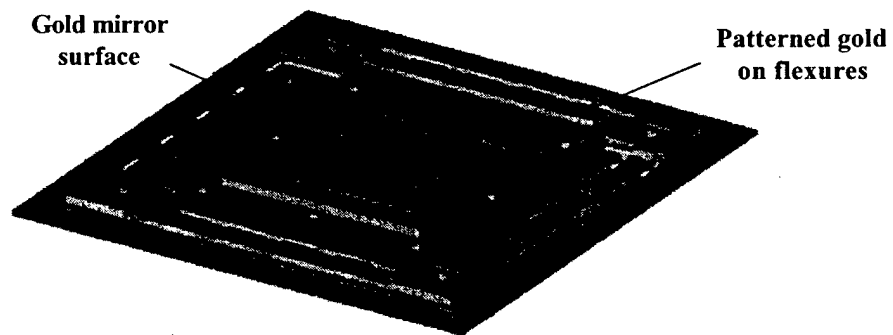


Figure 62. MEMCAD model of improved micromirror design using segmented gold on flexures.

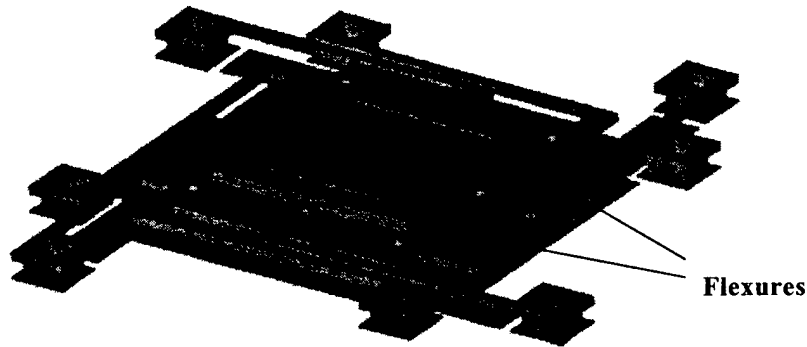


Figure 63. MEMCAD model of improved micromirror design using increased number of flexures.

Figure 64 shows the simulation results of the reduction of surface temperature with these two methods. The surface temperature is reduced from 325°C to 229°C (=96°C) if a segmented gold layer is patterned on flexures and laser power used is equal to 50 mW. Under the same condition, the surface temperature of micromirrors is reduced from 325°C to 276 °C (=49°C) if two flexures are used instead of one flexure along each side of the mirror. Therefore using segmented gold on flexures is a more effective method to reduce surface temperature than changing flexure design.

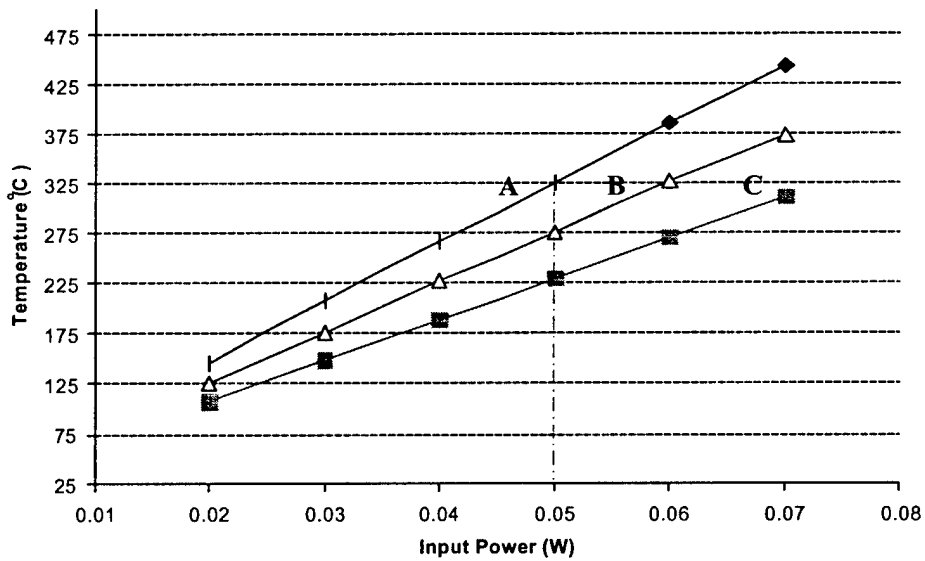


Figure 64. Reduction of surface temperature with improved micromirror designs
 (A: Original design, B: Two flexures along with each side, C: Gold on flexures)

6.3 Electrical-Mechanical Coupled Analysis

In order to evaluate the electrical-mechanical performance of improved design, finite element models were established by the use of MEMCAD. Figure 65 shows the displacement distribution of micromirrors when 10 volts are applied between top electrode and bottom electrode. From the results of the model, the pull-in voltage is 13 volts for the original design, which is in agreement with experimental result of 11.5 volts.

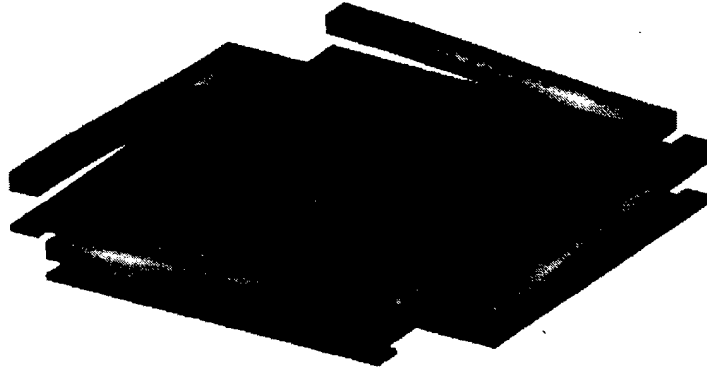


Figure 65. Electrical-mechanical model.

Figure 66 shows the experiment results of mechanical performance of micromirror for different designs. From this figure, we see that the two improved micromirror designs have similar mechanical behavior as the original design.

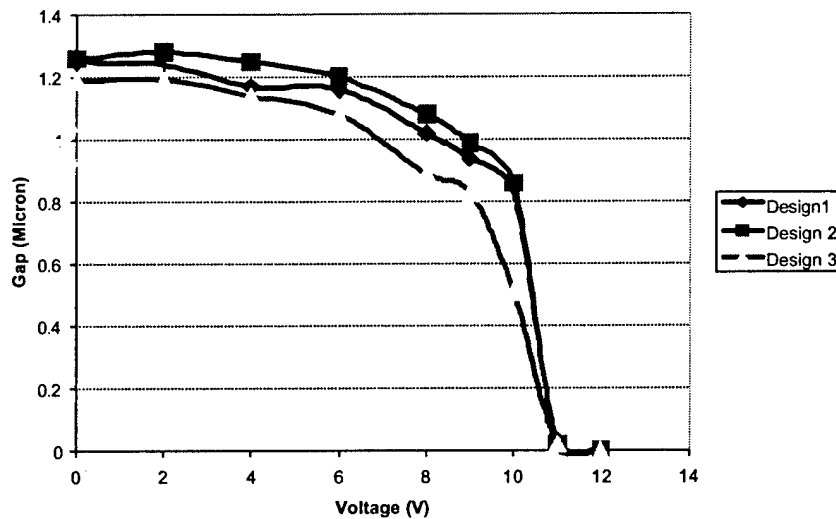


Figure 66. Mechanical behavior for micromirrors.

(Design 1: original design; Design 2: gold on flexures; Design3: two flexures along each side of the mirror)

6.4 Optical Experimental Results

The optical experiment setup, shown in Figure 67, was used to test the micromirror ability to handle the laser power. Laser wavelength of 830 nm was focused on the targeted micromirror (just on the reflective surface of the micromirror). Laser power level was pre-calibrated with an optical power meter. MEMS micromirror was placed in a vacuum chamber to test the power handling in low gas pressure environment.

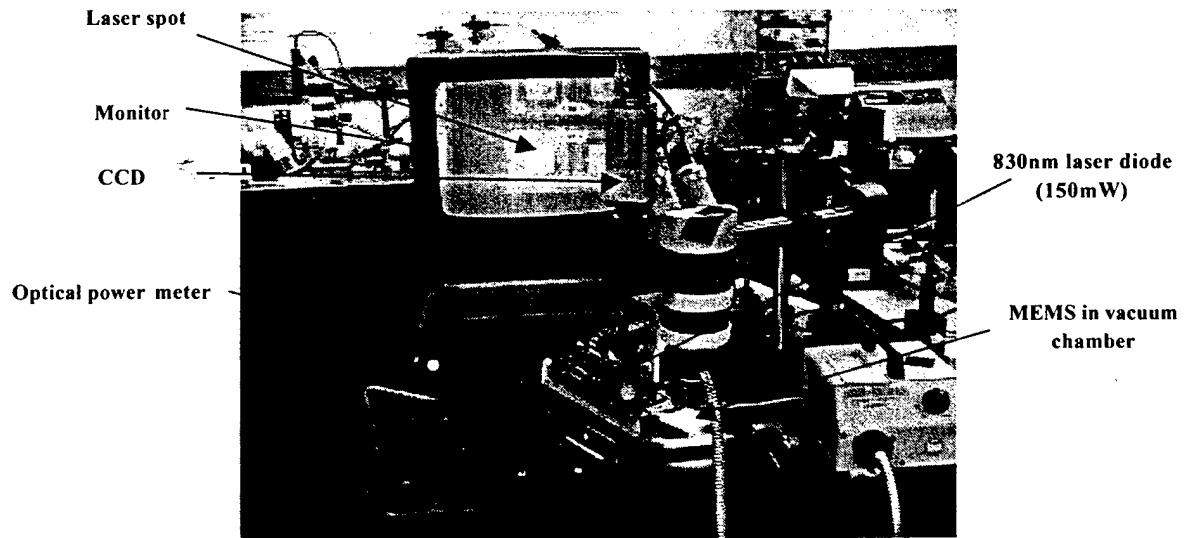
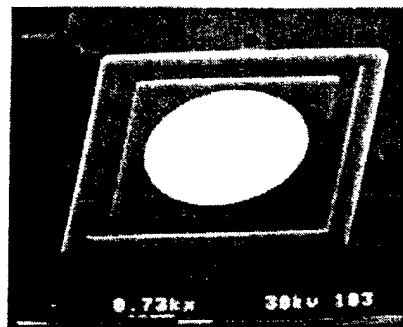


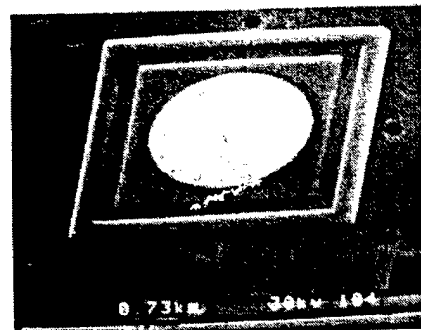
Figure 67. The optical experimental setup for laser power handling test.

The first reflectivity change of the micromirror was noticed at 70.74 mW. Eutectic bond between gold and polysilicon occurs at this heat flux. Afterward, the micromirror is destroyed in less than 30 seconds. Figure 68 shows the sequence of laser power damage for micromirror as the laser power is increased. In Figure 68(a), the gold surface of micromirror is clean and smooth when no laser power is applied. When laser power is increased to a certain level, the gold surface starts to react with polysilicon and looks rough as shown in Figure 68(b). Figure 68(c) shows the reaction of gold is growing when laser power is increased further. Then the gold is completely reacted and all the gold on micromirror is gone as shown in Figure 68(d). The same procedure was used to test all micromirrors, both original design and improved design. The fail power of micromirror is determined as the laser power at which the gold on micromirror starts reacting, as shown in Figure 68(b). Table 4 shows the experimental measurement of fail power for all micromirror designs.

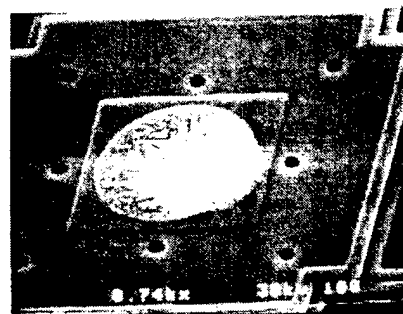
The measured fail power of design A (flexure made of Poly1, one flexure on each side of micromirror, and no gold deposited on flexures), 58.5 mW, is close to the predicted value of 52.3 mW. And the measured fail power of design D (flexure made of Poly1, two flexures on each side of micromirror, and no gold deposited on flexures), 91 mW, is close to the predicted value of 80.7 mW. Thus the experimental results are verified with the simulation results.



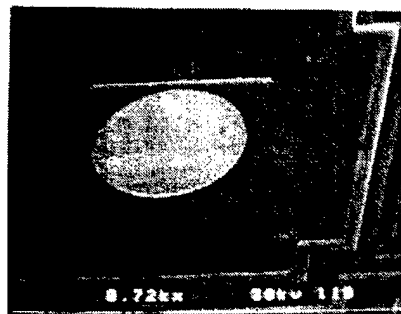
(a)



(b)



(c)



(d)

Figure 68. The sequence of laser induced damaged.

Table 4. Measured Fail Power of All Micromirror Designs.

Design	Measured Fail power (mW)
A	58.5
B	45.6
C	72.5
D	72.6
E	91
F	109.1

Note:

Design A = Original design (flexure made of Poly1, one flexure on each side of micromirror, and no gold deposited on flexures)

Design B = Original design (flexure made of Poly2, one flexure on each side of micromirror, and no gold deposited on flexures)

Design C = Improved design (flexure made of Poly2, one flexure on each side of micromirror, and gold deposited on flexures)

Design D = Improved design (flexure made of Poly2, two flexures on each side of micromirror, and no gold deposited on flexures)

Design E = Improved design (flexure made of Poly1, two flexures on each side of micromirror, and no gold deposited on flexures)

Design F = Improved design (flexure made of Poly2, two flexures on each side of micromirror, and gold deposited on flexures)

From Table 4, the fail power of design B is lower than of design A because the Poly2 layer (1.5 μm) is thinner than Poly1 layer (2 μm). Thus the cross section area of flexure in design A is larger than the cross section area of flexure in design B. With gold segment deposited on flexure of design C, the fail power of design C is significantly increased compared to design B. The gold segment layer enhances the heat conductivity of polysilicon flexure without the stress introduction to flexure. With increased number of flexures on each side of micromirror to two flexures per side, the fail power of design D is also significantly increased to the same level of design C. The design E is improved from design D by using Poly1 for the flexure, so the fail power of design E is further increased from design D due to the larger cross section area of the flexure. Finally, the fail power of design F is maximized by using two flexures on each side of micromirror and gold segments deposited on all the flexures.

6.5 SUMMARY

Thermal analysis of micromirror designs were investigated. The results of study were used to improve the design procedure of micromirrors. High power micromirrors were designed by using the modification of flexures that are the critical thermal path for low gas pressure. The low gas pressure environment is necessary for high frequency operation of micromirrors. Two methods for improved mirror designs were used, the gold segments deposited on flexures and the increased number of flexures per side of micromirror. These designs enhance the thermal conductivity through the flexures without interfering with the mechanical performance of micromirrors. Finite element models and experimental results confirm the improved optical power handling abilities of all micromirrors.

Published paper:

- J. L. Zhang, V.M. Bright, and Y.C. Lee, "Thermal interaction between laser and micromirrors," *Spatial Light Modulators and Integrated Optoelectronic Arrays (OSA)*, pp.111-113, 1999.

PERSONNEL

Investigators: Dr. Victor M. Bright, Principal Investigator; Dr. Y. C. Lee, Co-Principal Investigator

Graduate Students: Mr. Adisorn Tuantranont; Mr. Jianglong Zhang

Professional Research Assistants: Mr. Wenge Zhang; Ms. Ann Geesaman

PUBLICATIONS

Journal Papers:

A. Tuantranont, V.M. Bright, J.L. Zhang, W. Zhang, J. Neff, and Y.C. Lee, "Beam steering using MEMS-controllable microlens array," to appear in *Sensors and Actuators Physical A*.

L.A. Liew, A. Tuantranont, and V.M. Bright, "Modeling of thermal actuation in a bulk-micromachined CMOS micromirror," *Microelectronics Journal*, vol. 31, pp. 791-801, 2000.

A. Tuantranont, L.A. Liew, V.M. Bright, W. Zhang, and Y.C. Lee, "Phase-only micromirror array fabricated by standard CMOS process," to appear in *Sensors and Actuators Physical A*.

M. C. Roggemann, V.M. Bright, B. M. Welsh, W. D. Cowan, and M. Lee, "Micro-electro-mechanical deformable mirrors for aberration control in optical systems", *Optical and Quantum Electronics*, vol. 31, pp. 451-468, 1999.

W.D. Cowan, M.K. Lee, B.M. Welsh, V.M. Bright, and M.C. Roggemann, "Surface micromachined segmented mirrors for adaptive optics," *IEEE Journal of Selected Topics in Quantum Electronics: Special Issue on Micro-Opto-Electro-Mechanical Systems (MOEMS)*, vol. 5, no. 1, pp. 90-101, Jan./Feb. 1999.

W.D. Cowan, M.K. Lee, B.M. Welsh, V.M. Bright, and M.C. Roggemann, "Optical phase modulation using a refractive lenslet array and microelectromechanical deformable mirror," *Optical Engineering*, Vol. 37, No. 12, pp. 3237-3247, Dec. 1998.

M.K. Lee, W.D. Cowan, B.M. Welsh, V.M. Bright, and M.C. Roggemann, "Aberration-correction results from a segmented microelectromechanical deformable mirror and a refractive lenslet array," *Optics Letters*, vol. 23, no. 8, pp. 645-647, April 15, 1998.

Books:

C. Bang, V.M. Bright, M. Mignardi, and D.J. Monk, "Packaging and Test for MEMS and Optical MEMS," a chapter in *Recent Advances in MEMS/MOEMS*, J. Rai-Choudhury, editor, SPIE Press, 2000.

V.M. Bright, editor, *Optical MEMS*, SPIE Press, Vol. MS 153, Feb. 1999.

V.M. Bright, "Surface Micromachined Optical Systems," Chapter 12, pp. 485-518, *Microengineering Aerospace Systems*, H. Helvajian, editor, The Aerospace Press, El Segundo, CA., 1999.

W.D. Cowan and V.M. Bright, "Surface Micromachined Deformable Mirrors," Chapter 8, pp. 249-272, in *Adaptive Optics Engineering Handbook*, R.K. Tyson, editor, Marcel Dekker, Inc., New York, NY, 1999.

Conferences:

A. Tuantranont, L.A. Liew, V.M. Bright, J.L. Zhang, W. Zhang, and Y.C. Lee, "Bulk-Etched Surface Micromachined and Flip-Chip Integrated Micromirror Array for Infrared Applications," IEEE/LEOS International Conference on Optical MEMS 2000, pp. 71-72, 2000.

A. Tuantranont, V.M. Bright, J.L. Zhang, W. Zhang, J. Neff, and Y.C. Lee, "MEMS-controllable microlens array for beam steering and precision alignment in optical interconnect systems," 2000 Technical Digest of Solid-state Sensors and Actuators Workshop, pp. 101-104, 2000.

A. Tuantranont, V.M. Bright, L.A. Liew, W. Zhang, and Y.C. Lee, "Smart phase-only micromirror array fabricated by standard CMOS process," IEEE MEMS 2000 Proc., Miyazaki, Japan, pp. 455-460, 2000.

A. Tuantranont, V.M. Bright, W. Zhang and Y.C. Lee, "Flip chip integration of lenslet arrays on segmented deformable micromirrors," *Symposium on Design, Test, and Microfabrication of MEMS/MOEMS*, Paris, France, SPIE Vol. 3680, pp. 668-678, 1999.

A. Tuantranont, V.M. Bright, W. Zhang and Y.C. Lee, "Packaging of lenslet array on micromirrors," *Photonics West' 99 International symposium on OPTOELECTRONICS '99 - Integrated Devices and Applications*, San Jose, California, USA, SPIE Vol. 3631, pp. 156-164, 1999.

A. Tuantranont, V.M. Bright, W. Zhang, J.L. Zhang and Y.C. Lee, "Self-aligned assembly of microlens arrays with micromirrors," *Symposium on Micromachining and Microfabrication '99*, Santa Clara, California, USA, SPIE Vol. 3878, pp. 90-100, 1999.

J.L. Zhang, V.M. Bright, and Y.C. Lee, "Thermal interaction between laser and micromirrors," *Spatial Light Modulators & Integrated Optoelectronic Arrays (OSA)*, pp. 111-113, Snowmass, April 12-14, 1999.

W.D. Cowan, M.K. Lee, V.M. Bright, and B.M. Welsh, "Evaluation of microfabricated deformable mirror systems," *Proc. SPIE: Adaptive Optical System Technologies*, vol. 3353, pp. 790-804, 1998.

Patents:

Invention Disclosure "Moving and Fixing MEMS-Controlled Microlens Array for Optical Alignments" A. Tuantranont, J. L. Zhang, W. Zhang, Y. C. Lee, and V. M. Bright, submitted to Office of Technology Transfer and Industry Outreach, University of Colorado at Boulder.

Invention Disclosure "Method for Integrating of Bulk and Surface Silicon Micromachining through Multi-User MEMS Process (MUMPS) and use thereof" A. Tuantranont, L. A. Liew, and V. M. Bright, submitted to Office of Technology Transfer and Industry Outreach, University of Colorado at Boulder.

M. A. Michalick, V.M. Bright, and J.H. Comtois, "Multi-motion micromirror," U.S. Patent No. 6,028,689, Feb. 22, 2000.

HONORS/AWARDS:

J.T. Butler, V.M. Bright, P.B. Chu, and R.J. Saia, "Adapting multichip module foundries for MEMS packaging," *Proc. International Conference and Exhibition on Multichip Modules and High Density Packaging - MCM'98, Denver, CO, April 15-17, 1998*, pp. 106-111.
Best Paper of Session Award. Best Paper of Conference Award.